frontiers in Earth Science

ORIGINAL RESEARCH
published: 14 January 2021
doi: 10.3389/feart.2020.606951

Columbite-Tantalite Group Mineral U-Pb Geochronology of Chaqiabeishan Li-Rich Granitic Pegmatites in the Quanji Massif, NW China: Implications for the Genesis and Emplacement Ages of Pegmatites

Tong Pan[1], Qing-Feng Ding[2], Xuan Zhou[2], Shan-Ping Li[3], Jie Han[3] and Long Cheng[2]*

[1]Bureau of Geological Exploration and Development of Qinghai Province, Xining, China, [2]College of Earth Sciences, Jilin University, Changchun, China, [3]Qinghai Geological Survey Institute, Xining, China

OPEN ACCESS

Edited by:
Chang-Zhi Wu,
Chang'an University, China

Reviewed by:
Rongqing Zhang,
Nanjing University, China
Yonggang Feng,
Chang'an University, China

***Correspondence:**
Qing-Feng Ding
dingqf@jlu.edu.cn

Specialty section:
This article was submitted to Economic Geology, a section of the journal Frontiers in Earth Science

Received: *16 September 2020*
Accepted: *16 November 2020*
Published: *14 January 2021*

Citation:
Pan T, Ding Q-F, Zhou X, Li S-P, Han J and Cheng L (2021) Columbite-Tantalite Group Mineral U-Pb Geochronology of Chaqiabeishan Li-Rich Granitic Pegmatites in the Quanji Massif, NW China: Implications for the Genesis and Emplacement Ages of Pegmatites. Front. Earth Sci. 8:606951. doi: 10.3389/feart.2020.606951

The Chaqiabeishan area is characterized by small Li-rich granitic pegmatites in the Quanji Massif (QM), northwest China. In this study, the columbite-tantalite group minerals (CGMs) from a typical Li-rich pegmatite dike were analyzed for major element contents using an EMPA (electron microprobe analyzer), for trace element contents using LA-ICP-MS (laser ablation-inductively coupled plasma mass spectrometry), and for ages using LA-ICP-MS U-Pb dating, respectively. The CGMs from the sample can be divided into two types, i.e., magmatic Type 1 and metasomatic Type 2. Although these two types of CGMs do not exhibit distinct major and trace element variations from core to rim within an individual grain, the Ta# values, Mn# values, and some trace element contents (such as Zr, Hf, W, and Sr) of Type 1 CGMs are distinct from those of Type 2 CGMs. The overall compositional changes from Type 1 CGMs to Type 2 CGMs are consistent with the typical evolutionary trend described for many lithium-cesium-tantalum (LCT) pegmatites and the complex spodumene trend described by Černý and Ercit (Bull. Mineral., 1989, 108, 499–532). The Type 2 CGMs have formed later and must be a metasomatic product of Type 1 CGMs. Eighteen Type 1 CGMs yielded a weighted mean $^{206}Pb/^{238}U$ age of 240.6 ± 1.5 Ma. The slight oscillatory zoning and/or sector zoning suggest that the dated Type 1 columbites have a magmatic origin. Thus, the crystallization ages of Type 1 columbites represent the emplacement ages of Li-rich pegmatites. One of the Type 2 CGMs yielded a $^{206}Pb/^{238}U$ age of 211.0 ± 4.7 Ma, which is hardly interpreted to be an age representing the later hydrothermal metasomatism, because one dataset has no apparent statistical significance. Therefore, our dating results can only indicate that the Li-rich pegmatite-forming melts were emplaced at approximately 240.6 Ma. Based on these results and previous studies of the 240–254 Ma granitoids in the QM, we conclude that the 240.6 Ma Li-rich granitic pegmatites, as well as 240–254 Ma granitoids in the QM, were both emplaced during the southward subduction of the Zongwulong Ocean Plate in the Late Permian to Middle Triassic.

Keywords: columbite-tantalite group minerals, U-Pb dating, Li-rich pegmatite, Chaqiabeishan, Quanji Massif

INTRODUCTION

The Chaqiabeishan area in Tianjun County in Qinghai Province is tectonically located in the Quanji Massif (QM) and is one of the most important granitic pegmatite fields for rare element (Li and minor amounts of Be, Nb, and Ta) resources in Western China. Recently, these Li-rich pegmatites have attracted increasing amounts of attention because of the global demand for lithium and the Li prospecting potential in this area. The exotic granitic pegmatite group, including spodumene-bearing granitic pegmatites, tourmaline-bearing granitic pegmatites, beryl-bearing granitic pegmatites, and barren granitic pegmatites, was likely formed through fractional crystallization of a granitic magma (Wang et al., 2020). Yet, recently reported 235.9 and 217.0 Ma U-Pb ages of zircons within pegmatites by Wang et al. (2020) indicate amphibolous ages as well as an amphibolous genetic link between the rare-element pegmatites and the nearby Triassic granitic pluton. Nevertheless, the interpretation of the U-Pb zircon ages reported for the rare-element pegmatites remains ambiguous due to radioactive damage to the mineral structure and the disturbance of the U-Pb isotope systematics by the high U and Th contents of the zircons within the granitic pegmatites (Yan et al., 2018). Thus, the development of a precise dating alternative for the granitic pegmatites is vital for achieving a more thorough understanding of the tectono-metallogenic evolution of these pegmatites and a better exploration of the presence of rare-element-bearing minerals. Therefore, the emplacement ages of the Li-rich pegmatites in the Chaqiabeishan region need to be robustly determined to reconstruct the timeframe of the pegmatite emplacement and to explore the genesis of the Li-rich pegmatites.

Columbite-tantalite group minerals (CGMs) are important sources of critical elements, i.e., Nb and Ta, in highly evolved granites and granitic pegmatites (Linnen et al., 2012; Linnen et al., 2014). CGMs are suitable for dating granitic pegmatites (Romer and Wright, 1992; Romer et al., 1996; Smith et al., 2004; Che et al., 2015; Kaeter et al., 2018; Yan et al., 2018; Feng et al., 2019; Che et al., 2019) because the compatibility of U is sufficiently high and that of Pb is very low in CGM lattices. Recent studies have shown that CGMs are mainly crystallized from pegmatite-forming melts or during metasomatism (e.g., Van Lichtervelde et al., 2007). Therefore, U-Pb dating of CGMs can provide reliable emplacement ages for granitic pegmatites while the problems regarding zircon U-Pb dating need better explanation for pegmatites (Feng et al., 2019). In particular, in situ dating techniques such as laser ablation inductively coupled plasma mass spectrometry (LA-ICP-MS) and SIMS (secondary ion mass spectrometer) are being increasingly applied to U-Pb dating of CGMs (Che et al., 2015; Kaeter et al., 2018; Yan et al., 2018; Feng et al., 2019; Che et al., 2019) because they can avoid uranium-rich inclusions (e.g., uraninite) that are commonly present in CGMs (Che et al., 2015).

In this study, we dated representative CGM-bearing Li-rich pegmatite dikes in the Chaqiabeishan area using LA-ICP-MS CGM U-Pb dating. Then, the U-Pb ages obtained for the CGMs were compared with the U-Pb zircon ages obtained in previous studies and were used to reconstruct the evolution and timing of the Li-rich pegmatites in the Chaqiabeishan area. Based on the new age data, the genesis of the Li-rich pegmatites was also discussed according to the (electron microprobe analysis) EMPA and LA-ICP-MS trace element analysis results for the studied CGMs.

GEOLOGIC BACKGROUND AND GEOLOGY OF PEGMATITES

Geologic Background

The Chaqiabeishan area is tectonically located in the Quanji Massif in the North Qaidam tectonic belt (NQTB) (Wang et al., 2020). The NQTB, which is a tectonic terrane located between the Qaidam Block to the south and the Qilian Block to the north, consists of three tectonic units: the QM to the north, the Tanjianshan volcanic zone in the middle, and the North Qaidam high pressure to ultrahigh pressure (HP-UHP) metamorphic belt to the south (**Figure 1A**) (Wang et al., 2018). The latter two units are collectively referred to as the Early Paleozoic northern subduction-collision complex, which is related to the Proto-Tethys Ocean (e.g., Liao et al., 2018; Wu et al., 2019). The 540–500 Ma Tanjianshan volcanic zone has been suggested to have formed from volcanic island-arc magmatism related to northward oceanic subduction (Song et al., 2014; Zhang et al., 2014a; Zhang et al., 2017; Song et al., 2018). Continuous northward subduction of the lower plate between 500 Ma and 440 Ma (Song et al., 2018) gave rise to further island-arc magmatism in the QM and formed a continental arc. The Proto-Tethys Ocean was most likely completely closed by approximately 440 Ma when the continent-continent collision became the dominant tectonic movement in the NQTB (Wang et al., 2018). The closure of the Proto-Tethys Ocean at this time is supported by the intrusion of a postcollisional gabbroic dike at approximately 423 Ma (Wang et al., 2018). To the north, the QM is bordered by the Qinghai Lake fault (e.g., Liao et al., 2014; Zhang et al., 2014b; Mustafa et al., 2016) and the Zongwulong tectonic belt (e.g., Wang et al., 2016; Pang et al., 2019; Wang et al., 2019; Wu et al., 2019), which separates the QM from the Paleozoic South Qilian belt. Then, the Zongwulong oceanic basin was developed along the Zongwulong tectonic belt during the Middle Carboniferous to Early Permian in response to the continental rifting of the northern margin of the QM (Peng et al., 2018). By the Late Permian to Middle Triassic, the Zongwulong oceanic plate had subducted obliquely southward under the QM, forming I-type granitoids with ages of 240–254 Ma in the Tianjun and Wulan areas (Guo et al., 2009; Peng et al., 2016; Peng et al., 2018; Wu et al., 2019). Concurrently, the Paleo-Tethys oceanic plate was subducted northward, forming numerous granitic intrusions with ages of 240–254 Ma in the eastern Kunlun area (Ding et al., 2014; Xiong et al., 2014; Ding et al., 2015). Finally, the Zongwulong oceanic basin was closed during an intracontinental collisional orogeny in the Late Triassic (Guo et al., 2009; Peng et al., 2016; Peng et al., 2018).

The QM is nearly NW-SE-trending, but is E-W trending locally. It is a long and narrow small remnant continental

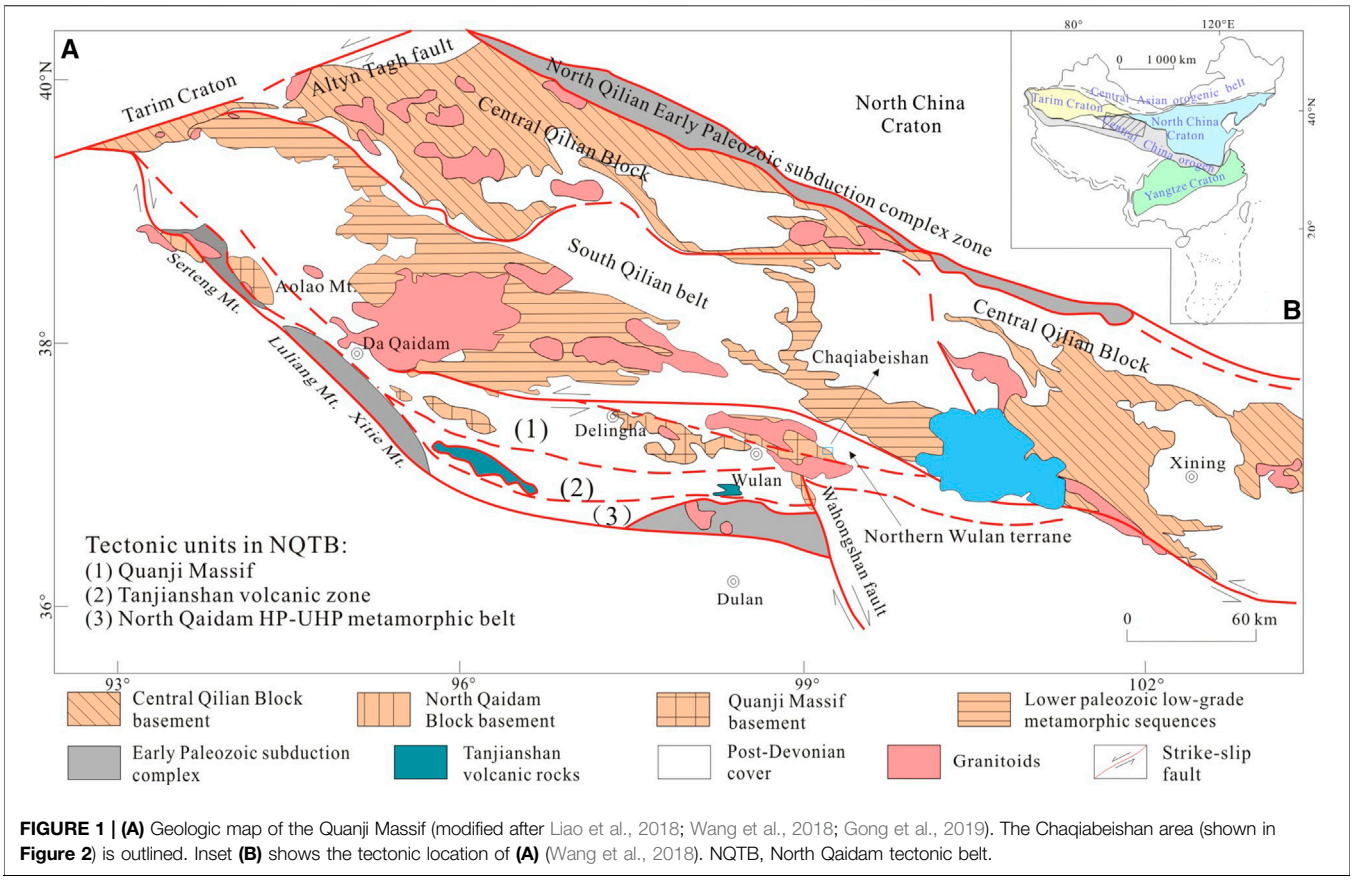

FIGURE 1 | (A) Geologic map of the Quanji Massif (modified after Liao et al., 2018; Wang et al., 2018; Gong et al., 2019). The Chaqiabeishan area (shown in **Figure 2**) is outlined. Inset **(B)** shows the tectonic location of **(A)** (Wang et al., 2018). NQTB, North Qaidam tectonic belt.

fragment, which was detached from the Tarim Craton (TC); so, the QM has had a geological history similar to that of the TC since the middle Neoproterozoic (Zhang et al., 2012). The QM is characterized by the components of a double-layered structure. The basement is composed of early Paleoproterozoic granitic gneisses and medium- to high-grade metamorphic rocks (e.g., Gong et al., 2012; Gong et al., 2014; Zhang et al., 2014b; Liao et al., 2018; Wang et al., 2018), and the cover is composed of Mesoproterozoic–Phanerozoic sedimentary rocks (Zhao et al., 2000; Lu et al., 2006; Lu et al., 2008; Zhang et al., 2012; Wang et al., 2016; Wang et al., 2018; Wang et al., 2019). The metamorphic basement of the QM is mainly composed of the early Paleoproterozoic Delingha complex and the amphibolite facies of the Paleoproterozoic Dakendaban Group paragneisses (Lu et al., 2008; Chen et al., 2012; Gong et al., 2012; Zhang C. L. et al., 2014; Gong et al., 2014; He et al., 2018; Gong et al., 2019), which is unconformably overlain by the sedimentary strata of the approximately 1.73–1.64 Ga Quanji Group (Zhang et al., 2017), and Upper Neoproterozoic and Lower Paleozoic to Mesozoic strata (Lu et al., 2008; Zhang et al., 2012; Zhang et al., 2016).

This study area is located in the eastern segment of the QM (**Figure 1A**). Some researchers have argued that the North Wulan terrane (NWT) can be separated from the northern QM (Wang et al., 2016; Pang et al., 2019; Wang et al., 2019; Wu et al., 2019). The NWT is bounded to the north by the Zongwulong tectonic belt, and it is separated from the QM to the south by a Cenozoic thrust fault (**Figure 1A**) (Xu et al., 2006; Chen et al., 2009; Guo et al., 2009; Xiao et al., 2009).

Geology of Chaqiabeishan Pegmatites

The Chaqiabeishan Li-rich pegmatites are located in the NWT within the QM (**Figure 1A**). The metamorphic basement of the study area is mainly composed of the Paleoproterozoic Dakendaban Group, which consists of the gneiss formation, the schist formation, and the marble formation. The basement is unconformably overlain by the unmetamorphosed Carboniferrous–Early Permian Ganjia Formation and the Early–Middle Triassic Zongwulong River Formation (Wang et al., 2020). The Gneiss Formation in the Dakendaban Group, which is located to southwest of the South Zongwulong Mountain fault (F4; **Figure 2**) (Wang et al., 2020), consists of amphibolite-facies felsic gneiss interbedded with minor mica schist and plagioclase amphibolite. Meanwhile, the schist formation in the Dakendaban Group, which is located to the northeast of fault F4, is composed of green-schist-facies mica schist. This schist is considered to be part of the Dakendaban Group by Wang et al. (2020), but there are some minor differences between the lithological assemblage and metamorphic degree of the schist and those of the Dakendaban Group in the southwestern part of the study area (Wang et al., 2020). The Carboniferrous–Early Permian Ganjia Formation and the Early–Middle Triassic Zongwulong River Formation are distributed from northwest

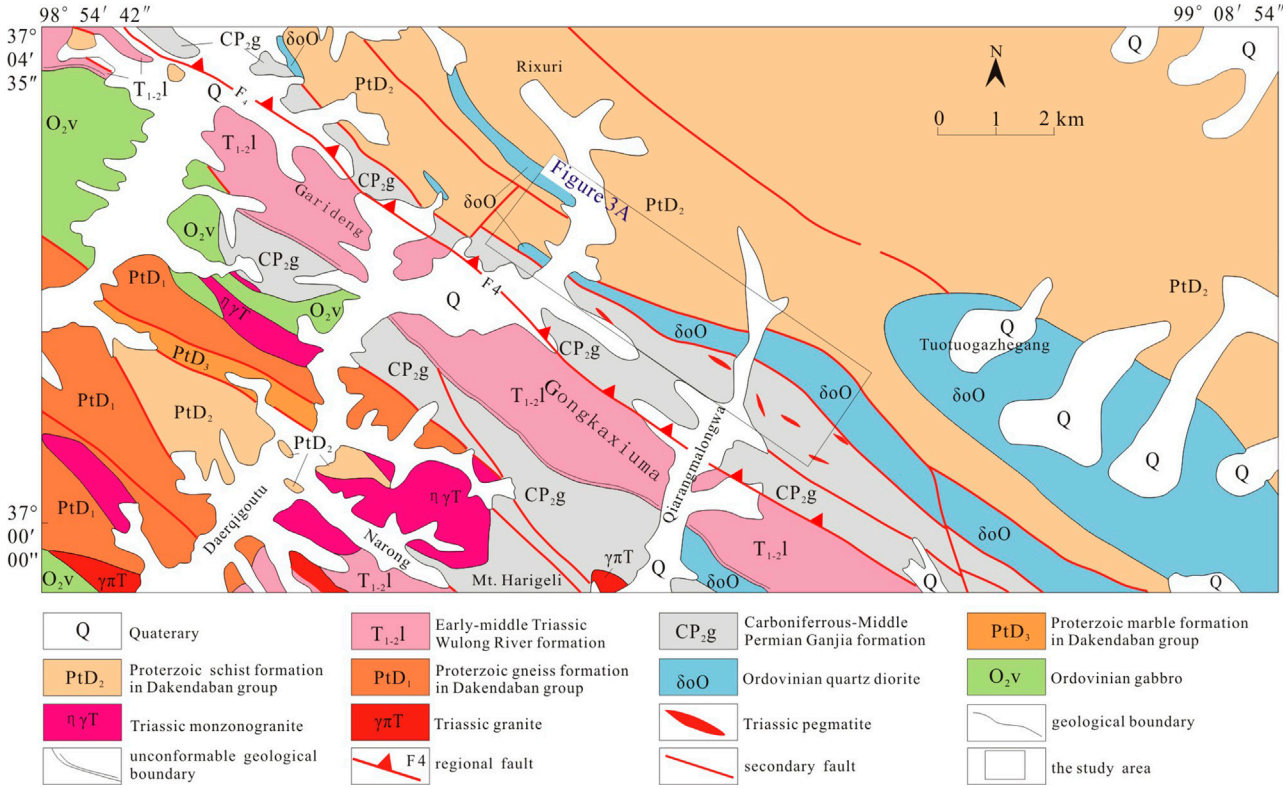

FIGURE 2 | Geologic map of the Chaqiabeishan area in the Quanji Massif (after Wang et al., 2020). The granitic rocks near the study area are also shown in the figure.

to southeast in the central region of the study area (**Figure 2**) (Wang et al., 2020). The Ganjia Formation is composed of lower sandstone and upper limestone, while the Zongwulong River Formation consists of a marine clastic-facies turbidite. Regional fault F4 strikes southeast and dips northeast, across the study area (**Figure 2**) (Wang et al., 2020). A series of secondary faults and miliolite zones are developed in the hanging wall of fault F4, and they are pegmatite-controlling structures in the study area. The intermediate-mafic intrusions include Ordovician gabbro and quartz diorite, with the gabbros mostly occurring in the northwestern part of the study area and the quartz diorites occurring in the southeastern part (**Figure 2**) (Wang et al., 2020). The quartz diorites were emplaced along the regional fault at approximately 440 Ma (QGSI, 2020), and they mostly strike northwest. Some of the granitic rocks in the southwestern part of the study area are considered to be emplaced in the Triassic or earlier. No previous studies have been conducted on these granitic rocks in the study area (**Figure 2**).

Numerous granitic pegmatite dikes were emplaced along the northwest-southeast-trending miliolite zones and the secondary faults within the quartz diorites and Dakendaban Group strata (**Figures 3**, **4A,B**) (Pan et al., 2020). These granitic pegmatites are lentoid or banded, are 5–60 m long and 0.2–20 m wide, and include spodumene-bearing pegmatites, tourmaline-bearing pegmatites, beryl-bearing pegmatites, and other barren pegmatites. Usually, the granitic pegmatites have a massive unzoned structure and a granitic composition, and they do not exhibit internal fractionation, zoning, or quartz cores (**Figures 4C,D**). Estimates of the pegmatite bulk compositions indicate that they are granitic, and that the abundances of the fluxing components (*B*, *P*, and *F*), rare alkalis (Li), alkaline earth metals (Be), and high field strength elements (HFSE) (Nb, Ta, and U) are significantly higher than in common granites (e.g., London, 2018). Some of the pegmatites have extremely high Li_2O values (>2.15 wt.%) and relatively high Be, Nb, and Ta contents. The mineralized pegmatites are Li-rich or Be-rich, among which 58 Li-Be ore bodies and 130 Li-Be mineralized bodies (i.e., the ore grades are lower than the cut-off grade) have been delineated (QGSI, 2020). Evidence in support of a petrogenetic link among the granites is not be provided by the field relationships. The granitic pegmatites are usually coarse-grained to pegmatitic (i.e., crystals mostly up to 10 cm long) and consist of 20–40% quartz, 5–25% plagioclase (primarily albite), 10–30% potassium feldspar (primarily perthite), 5–30% spodumene, 5–15% tourmaline, <5% muscovite (and/or lepidolite), <5% beryl, and <5% garnet (**Figures 4C–F**). The accessory minerals include zircon, phosphorite, and CGMs.

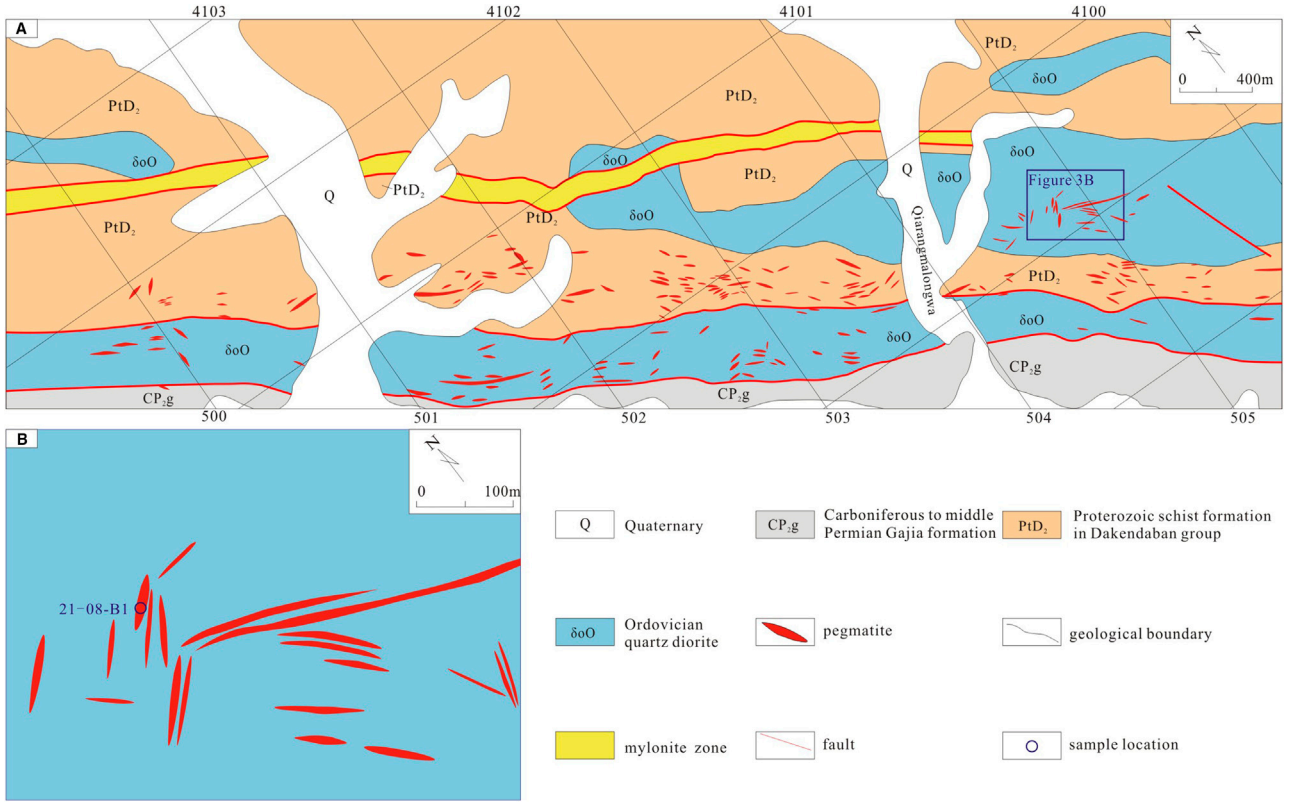

FIGURE 3 | (A) Geologic map of the Chaqiabeishan Li-rich pegmatite area (after Wang et al., 2020). **(B)** Geologic map of the typical CGM-bearing Li-rich pegmatites in the Chaqiabeishan area. Sample location of the CGMs used for the dating is also shown in this figure.

SAMPLING AND METHODS

Sampling and Imaging

The Li-rich pegmatites in the southwestern part of the Chaqiabeishan area (**Figure 3A**) have relatively high Nb and Ta contents, and we believe that CGMs occur in such Li-rich pegmatites. Doubly polished thin sections were made from the rock samples collected from ten typical pegmatite dikes in the study area for the petrographic study. CGMs grains were successfully separated from the sample CQBS21-08-B1, which was collected from a typical Li-rich pegmatite dike in the study area (**Figure 3B**). The CGMs grains were mounted in epoxy resin and polished for EMPA analysis, LA-ICP-MS dating, and LA-ICP-MS trace element analysis. Back-scattered electron (BSE) images of the doubly polished thin sections were obtained using the TESCAN MIRA 3 LMH scanning electron microscope (SEM) at Nanjing Hongchuang Exploration Technology Service Co., Ltd.

Electron Microprobe Analyzer

The mineral compositions were analyzed at the Wuhan Microbeam Analysis Technology Co., Ltd., using a JEOL JXA-8230 electron microprobe analyzer equipped with five wavelength-dispersive spectrometers (WDS). First, the samples were coated with a thin conductive carbon film prior to analysis. The precautions suggested by Zhang and Yang (2016) were used to minimize the variations in the carbon film thickness between the samples and to obtain an approximately 20 nm thick, uniform coating. The operating conditions for the quantitative WDS analyses involved an accelerating voltage of 15 kV, a beam current of 20 nA, and a spot size of 1.0 μm. The peak counting time was 10 s for W, Ca, Ti, Ta, Nb, Al, and Sn and 20 s for Fe and Mn. The background counting time was 1/2 of the peak counting time for the high- and low-energy background positions. The following standards were used: tungsten (W), diopside (Ca), ilmenite (Ti), tantalum (Ta), niobium (Nb), tin (Sn), pyrope garnet (Fe and Al), and rhodonite (Mn).

Laser Ablation-Inductively Coupled Plasma Mass Spectrometry U-Pb Dating and Trace Element Analysis

The LA-ICP-MS U-Pb dating and in situ trace element analysis of the CGMs were simultaneously conducted at the State Key Laboratory for Mineral Deposits Research, Nanjing University, China, using the analytical procedures described in detail by Che et al. (2015). A Photon Machines Excite laser ablation system

FIGURE 4 | Photographs and photomicrographs showing the morphology and textural features of the spodumene-rich pegmatites in the Chaqiabeishan area. **(A)** The pegmatite dike was intruded along the bedding of the gneiss strata. **(B)** Sharp contacts between pegmatites and quartz diorites. **(C)** The spodumene in the pegmatite dikes is characterized by pegmatitic texture. **(D)** Coexistence of pegmatitic spodumene, tourmaline, plagioclase, and quartz in the pegmatite specimen. **(E)** Coexisting pegmatitic euhedral spodumene, subhedral plagioclase, and coarse-grained anhedral quartz under plane-polarized transmitted light. **(F)** Coexisting pegmatitic euhedral spodumene, subhedral plagioclase, and coarse-grained anhedral quartz under perpendicular polarized transmitted light. Spd, spodumene; Qz, quartz; Pl, plagioclase; Tur, tourmaline.

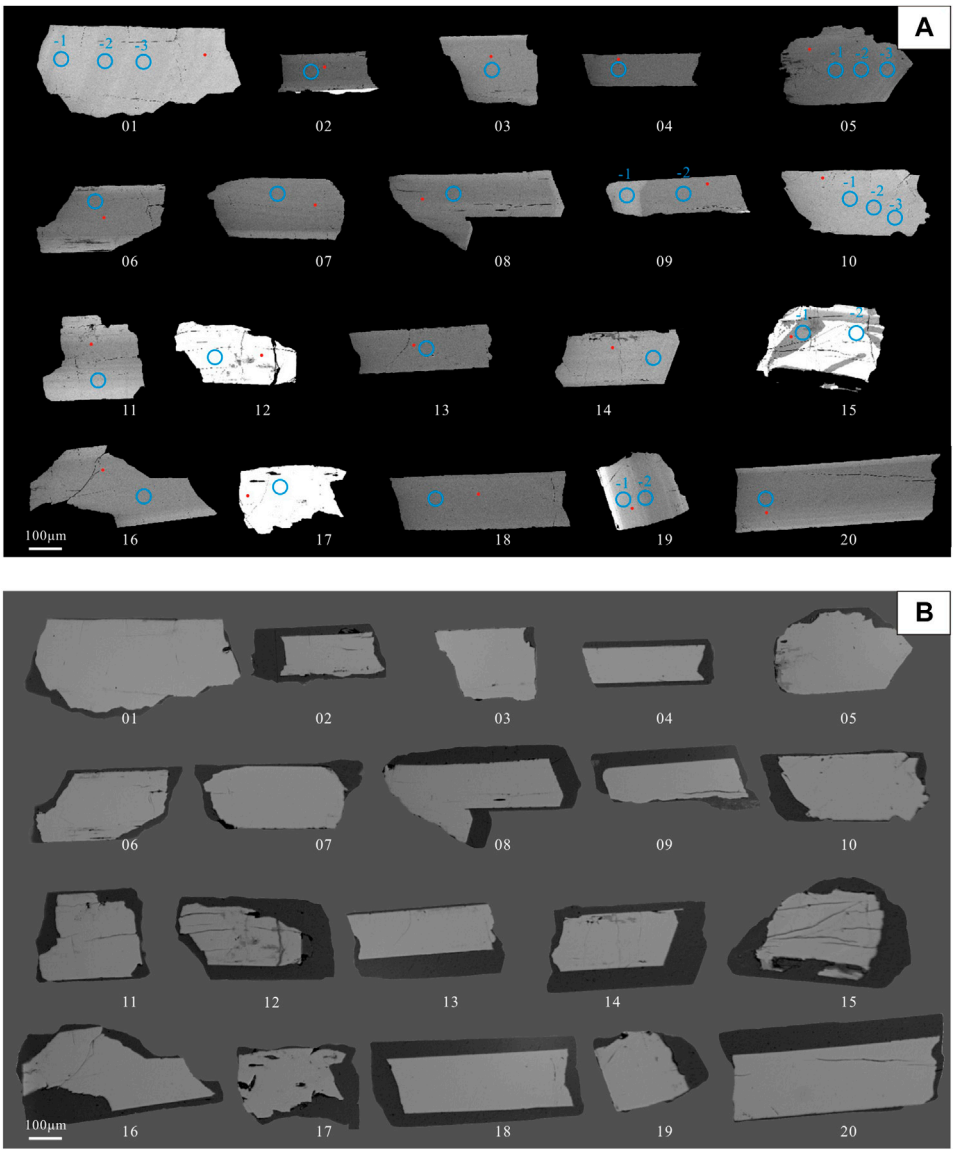

FIGURE 5 | (A) BSE images and **(B)** plane-polarized reflected light photomicrographs of representative analyzed CGM separates from the Li-rich pegmatites in the Chaqiabeishan area. The blue circles represent the positions of the 43 μm ablation spots from the LA-ICP-MS dating and trace element analysis. The red dots represent the positions of the 1.0 μm EMPA spots. The scale bars are 100 μm long.

(RESOlution S-155) integrated with an inductively coupled plasma-mass spectrometer (Thermo Fisher Scientific i-CAP-Q) was used for the analyses. The ablation protocol included a spot diameter of 43 μm and a repetition rate of 4 Hz for 40 s. Helium was applied as the carrier gas to efficiently transport the aerosol into the ICP-MS. Coltan 139 with a weighted mean $^{207}Pb/^{206}Pb$ age of 506 ± 2.3 Ma (obtained by isotope dilution thermal ionization mass spectrometry) and an LA-ICP-MS U-Pb age of 506.2 ± 5.0 Ma (Che et al., 2015 and references therein) was used as the external standard for calibrating the U, Th, and Pb isotopic ratios. US National Institute of Standards and Technology (NIST) standard reference materials NIST-610 and NIST-612 and US Geological Survey basaltic glasses BCR-2G and GSE-1G were used as additional external standards to plot the calibration curve (Gao et al., 2013). ^{55}Mn was used as an internal standard for calibrating trace element concentrations (Che et al., 2015). Every eight analyses were followed by the analysis of two NIST SRM 610 measurements, one GSE-1G measurement, one BCR-2G measurement, and two Coltan139 measurements. Each spot analysis consisted of approximately 20 s of background acquisition, 50 s of sample data acquisition, and up to 20 s of gas blank acquisition to flush the sample. The offline data processing was performed using the ICPMSDataCal program (Liu et al., 2008). The concordia U-Pb ages were calculated using the Isoplot 3.0 software (Ludwig, 2003). The estimated precision is better than ±5% for the major elements and ±10% for the trace elements (Xie et al., 2019).

TABLE 1 | Results of EPMA for CGMs in the Chaqiabeishan area.

Spot no.	B1-1	B1-2	B1-3	B1-4	CB1-5	-B1-6	B1-7	B1-8	B1-9	B1-10	B1-11	B1-12	B1-13	B1-14	B1-15-1	B1-15-2	B1-16	B1-17	B1-18	B1-19	B1-20
CGM type	**Type 1**	**Type 1**	**Type 1**	**Type 1**	**Type 1**	**Type 1**	**Type 1**	**Type 1**	**Type 1**	**Type 1**	**Type 1**	**Type 2**	**Type 1**	**Type 1**	**Type 1**	**Type 2**	**Type 1**	**Type 2**	**Type 1**	**Type 1**	**Type 1**
Al2O3 wt.%	0.003	0.027	0.001	b.d.l.	b.d.l.	0.032	b.d.l.	0.009	b.d.l.	0.012	0.009	0.027	b.d.l.	b.d.l.	b.d.l.	b.d.l.	b.d.l.	b.d.l.	b.d.l.	0.006	0.010
WO3	1.386	0.849	1.023	0.824	1.068	1.200	0.800	0.887	1.200	1.110	1.039	1.871	1.195	1.067	0.955	1.860	1.213	2.119	0.897	0.814	0.998
TiO2	2.203	1.703	1.848	1.771	1.818	2.008	1.597	1.704	1.138	1.766	2.181	1.069	1.972	1.860	1.506	0.730	2.002	0.941	2.074	1.828	1.578
Ta2O5	36.505	23.782	27.469	23.281	26.278	27.255	27.274	24.506	27.512	32.026	28.813	54.353	22.745	27.997	26.986	53.610	26.421	57.196	23.007	30.149	25.339
FeO	3.966	5.834	4.412	5.919	5.172	4.467	4.767	5.852	4.608	3.721	4.183	2.214	5.596	4.841	4.686	2.310	4.477	2.868	5.437	4.321	5.288
CaO	0.005	0.035	0.005	0.016	b.d.l.	0.010	0.018	0.013	0.062	0.061	0.000	0.138	0.014	0.262	0.018	0.070	0.004	b.d.l.	0.008	0.015	0.017
MnO	13.767	13.224	14.383	13.259	13.506	14.193	13.997	13.080	13.791	14.015	13.670	13.780	12.636	13.679	13.677	14.230	14.337	13.465	12.700	14.629	13.503
SnO2	0.605	0.708	0.670	0.778	0.490	0.670	0.457	0.640	0.378	0.503	0.558	0.525	0.584	0.438	0.521	0.340	0.626	0.711	0.814	0.689	0.460
Nb2O5	40.905	52.366	49.423	53.003	51.375	50.103	51.162	53.536	50.348	45.838	47.791	25.659	53.490	49.582	50.738	26.740	49.844	22.914	53.324	46.484	52.225
Total	99.345	98.528	99.234	98.851	99.707	99.938	100.072	100.227	99.037	99.052	98.244	99.636	98.232	99.726	99.087	99.890	98.924	100.214	98.261	98.935	99.418
Based on 6 O atoms																					
Al apfu	0.000	0.002	0.000	0.000	0.000	0.002	0.000	0.001	0.000	0.001	0.001	0.002	0.000	0.000	0.000	0.000	0.000	0.000	0.000	0.000	0.001
W	0.024	0.014	0.017	0.013	0.017	0.020	0.013	0.014	0.020	0.019	0.017	0.035	0.019	0.017	0.016	0.035	0.020	0.040	0.015	0.014	0.016
TiO2	0.109	0.081	0.088	0.083	0.086	0.095	0.075	0.079	0.055	0.086	0.106	0.058	0.093	0.088	0.072	0.039	0.095	0.052	0.098	0.089	0.074
Ta	0.655	0.407	0.474	0.396	0.448	0.466	0.465	0.413	0.477	0.564	0.504	1.067	0.388	0.481	0.465	1.047	0.456	1.135	0.392	0.529	0.432
Fe	0.219	0.307	0.234	0.310	0.271	0.235	0.250	0.303	0.246	0.202	0.225	0.134	0.294	0.256	0.248	0.139	0.237	0.175	0.285	0.233	0.277
Ca	0.000	0.002	0.000	0.001	0.000	0.001	0.001	0.001	0.004	0.004	0.000	0.011	0.001	0.018	0.001	0.005	0.000	0.000	0.001	0.001	0.001
Mn	0.770	0.705	0.773	0.703	0.718	0.755	0.744	0.686	0.744	0.769	0.745	0.842	0.671	0.732	0.734	0.866	0.770	0.832	0.674	0.799	0.717
Sn	0.016	0.018	0.017	0.019	0.012	0.017	0.011	0.016	0.010	0.013	0.014	0.015	0.015	0.011	0.013	0.010	0.016	0.021	0.020	0.018	0.012
Nb	1.220	1.490	1.418	1.500	1.457	1.424	1.451	1.498	1.450	1.343	1.390	0.837	1.516	1.416	1.454	0.868	1.429	0.756	1.512	1.356	1.481
O	6.000	6.000	6.000	6.000	6.000	6.000	6.000	6.000	6.000	6.000	6.000	6.000	6.000	6.000	6.000	6.000	6.000	6.000	6.000	6.000	6.000
Mn#	77.853	69.655	76.751	69.405	72.561	76.290	74.833	69.358	75.191	79.228	76.795	86.307	69.574	74.103	74.720	86.185	76.432	82.622	70.287	77.419	72.113
Ta#	34.931	21.457	25.056	20.900	23.529	24.655	24.281	21.590	24.738	29.591	26.614	56.029	20.368	25.354	24.239	54.669	24.177	60.024	20.606	28.065	22.592
A	1.138	1.129	1.130	1.130	1.104	1.125	1.095	1.100	1.078	1.094	1.108	1.097	1.093	1.122	1.085	1.094	1.139	1.120	1.093	1.154	1.099
B	1.876	1.898	1.892	1.896	1.905	1.889	1.917	1.911	1.927	1.908	1.895	1.904	1.904	1.897	1.920	1.915	1.884	1.891	1.904	1.885	1.913

Note: b.d.l., below detection limit. "CQBS21-08-B1" within spot no. was abbreviated as "B1" in each one.

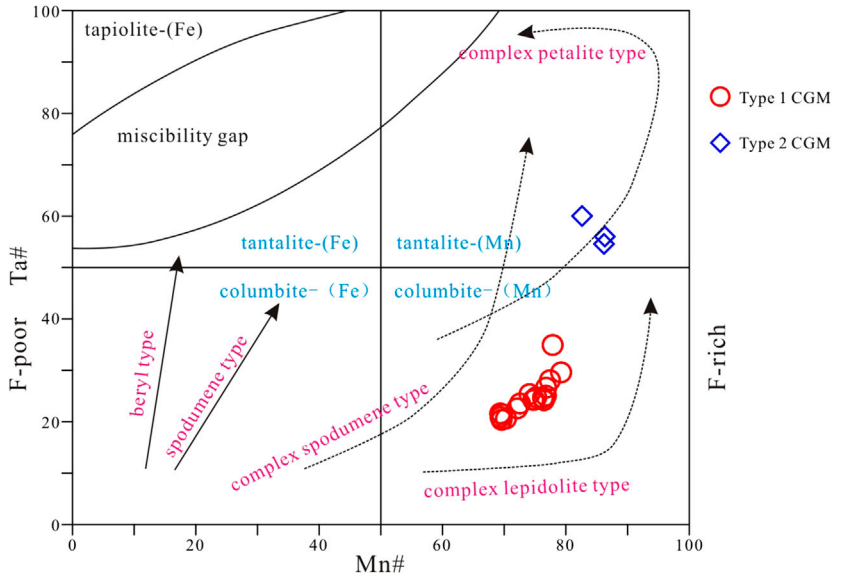

FIGURE 6 | Ta# vs. Mn# quadrilateral diagram (Černý and Ercit, 1989) for the CGMs from the Li-rich pegmatites in the Chaqiabeishan area. The Ta and Mn enrichment trends of CGMs in fluorine-rich and fluorine-poor pegmatites are also based on Černý and Ercit (1989).

RESULTS

Petrography and Classification of CGMs

CGMs were not directly observed within two of the doubly polished thin sections of the investigated pegmatites perhaps because the small CGMs had grain sizes of 150–500 μm. However, many CGM grains were successfully separated from the pegmatite sample CQBS21-08-B1 whose Nb and Tb abundances are up to 144.5 ppm and 79.9 ppm, respectively (unpublished data). We believe that CGMs are paragenetic with the other rare-element-rich minerals in the Li-rich pegmatites because recent studies have shown that CGMs mainly crystallize from pegmatite-forming melts or during metasomatism (Van Lichtervelde et al., 2007). The CGM separates were generally euhedral to subhedral and gray in plane-polarized reflected light (**Figure 5B**). The BSE images showing all of the analytical spots for the in situ LA-ICP-MS dating, trace element analysis, and EMPA are presented in **Figure 5A**. Two types of CGMs were identified based on their morphology and BSE images (**Figure 5**). The BSE images show that most of the Type 1 CGMs have dark BSE images and weak sector zoning or minor oscillatory zoning (**Figure 5A**), indicating that they are typical magmatic CGMs (Badanina et al., 2015; Van Lichtervelde et al., 2007; Timofeev et al., 2017), since oscillatory zoning is believed to be the result of the slow diffusion of Ta and Nb in the melt relative to the rate of crystal growth (Van Lichtervelde et al., 2007). The Type 2 CGMs have irregular or complicated internal textures, some of which have both bright patches and dark patches in the BSE images (e.g., nos. 12, 15, and 17 in **Figure 5A**), indicating that they are perhaps related to late-stage metasomatic replacement caused by highly reactive fluids exsolved from the residual melts (Černý and Ercit, 1985; Tindle and Breaks, 2000; Badanina et al., 2015).

Electron Microprobe Analyzer

All of the analyzed CGMs contain 2.214–5.919 wt.% FeO, 12.636–14.629 wt.% MnO, 0.730–2.203 wt.% TiO_2, and 0.0800–2.119 wt.% WO_3. The Al_2O_3, CaO, and SnO_2 contents are mostly less than 0.800 wt.% (**Table 1**). However, their Nb_2O_5 and Ta_2O_5 contents are variable. Eighteen of the analyzed spots on the CGMs separates with dark BSE images (including a residual dark patch in CGM grain no. 15-1), i.e., Type 1 CGMs, are compositionally columbite-(Mn) with relatively similar low Ta# values; while three of the CGMs (nos. 12, 15-2, and 17) with bright BSE images, i.e., the Type 2 CGMs, are compositionally tantalite-(Mn) with higher Ta# values (**Table 1**, **Figures 5** and **6**).

Laser Ablation-Inductively Coupled Plasma Mass Spectrometry U-Pb Dating

The LA-ICP-MS U-Pb dating data for the CGMs are presented in **Table 2**. Twenty-nine spots on 20 CGM grains from the same Li-rich pegmatite (sample CQBS21-08-B1) were analyzed. **Figure 5** shows all of the dated CGM grains and analytical spots. Some of the data points plot below the concordia line, suggesting potential Pb loss, which could be caused by metamictization (Romer, 2003). Most disconcordant dating analyses show extremely high common Pb concentrations (up to 5,981.35 ppm; **Table 2**), indicating that the influence of common Pb is also very significant and that microscale U-rich inclusions (e.g., feldspar) is possibly present in some of the CGMs analyzed (e.g., Romer, 2003; Legros et al., 2019). Certainly, other reasons for high common Pb in CGMs may be possible. Moreover, the BSE images show that the discordant ages are likely caused by the presence of microfractures close to

TABLE 2 | LA-ICP-MS dating results for CGMs in the Chaqiabeishan area.

Spot no.	^{232}Th	^{238}U	Total Pb	Common Pb	Isotopic ratios						Isotopic ages (Ma)						Concordance
	(ppm)	(ppm)	(ppm)	(ppm)	207*Pb*/206*Pb*	1σ	207*Pb*/235*U*	1σ	206*Pb*/238*U*	1σ	207*Pb*/206*Pb*	1σ	207*Pb*/235*U*	1σ	206*Pb*/238*U*	1σ	
B1-1-1	77.8	7478.0	289.5	0.8	0.050895	0.000310	0.266870	0.004915	0.038091	0.000681	235.3	14.8	240.2	3.9	241.0	4.2	99%
B1-1-2	75.5	7080.4	277.8	0.8	0.050279	0.000321	0.264209	0.004903	0.038173	0.000691	209.3	19.4	238.1	3.9	241.5	4.3	98%
B1-1-3	93.1	7597.8	302.1	0.0	0.050332	0.000301	0.268238	0.004967	0.038721	0.000700	209.3	17.6	241.3	4.0	244.9	4.3	98%
B1-2	23.7	2279.9	100.8	13.8	0.078636	0.001782	0.413782	0.010412	0.038174	0.000362	1164.8	45.2	351.6	7.5	241.5	2.2	62%
B1-3	27.9	2632.4	104.2	1.0	0.050070	0.000431	0.264841	0.004322	0.038406	0.000554	198.2	13.9	238.6	3.5	242.9	3.4	98%
B1-4	53.1	4614.0	183.2	0.7	0.050611	0.000350	0.264879	0.002763	0.037995	0.000328	233.4	16.7	238.6	2.2	240.4	2.0	99%
B1-5-1	77.5	4951.5	195.4	0.0	0.050510	0.000315	0.265755	0.003963	0.038210	0.000544	216.7	10.2	239.3	3.2	241.7	3.4	98%
B1-5-2	76.7	4564.6	180.9	0.4	0.050845	0.000309	0.269870	0.004414	0.038448	0.000557	235.3	17.6	242.6	3.5	243.2	3.5	99%
B1-5-3	73.5	4028.5	159.8	1.2	0.050150	0.000346	0.265448	0.004865	0.038410	0.000655	211.2	14.8	239.0	3.9	243.0	4.1	98%
B1-6	41.9	1727.5	294.4	208.1	0.345648	0.011731	3.829526	0.197022	0.074317	0.002299	3688.0	51.8	1599.0	41.4	462.1	13.8	-11%
B1-7	25.7	2444.9	147.9	26.0	0.100916	0.001213	0.666591	0.010256	0.048106	0.000659	1642.6	22.2	518.6	6.3	302.9	4.1	47%
B1-8	38.5	3437.4	136.3	0.7	0.051094	0.000355	0.267687	0.004323	0.037999	0.000561	255.6	16.7	240.8	3.5	240.4	3.5	99%
B1-9-1	72.5	4829.0	227.9	27.7	0.077165	0.003487	0.474811	0.028543	0.041528	0.000805	1125.6	90.3	394.5	19.7	262.3	5.0	59%
B1-9-2	14.2	1687.7	95.4	34.4	0.145555	0.003498	0.824982	0.030801	0.040188	0.000762	2294.1	40.6	610.8	17.1	254.0	4.7	17%
B1-10-1	29.1	2724.6	108.7	0.6	0.050688	0.000376	0.264255	0.004130	0.037796	0.000530	233.4	16.7	238.1	3.3	239.2	3.3	99%
B1-10-2	36.9	3090.4	123.3	0.4	0.050182	0.000385	0.262699	0.004055	0.037967	0.000535	211.2	16.7	236.8	3.3	240.2	3.3	98%
B1-10-3	30.3	2799.3	112.3	0.9	0.050828	0.000435	0.260533	0.003798	0.037161	0.000473	231.6	20.4	235.1	3.1	235.2	2.9	99%
B1-11	91.2	7000.7	280.3	0.8	0.050864	0.000303	0.265347	0.004449	0.037791	0.000604	235.3	17.6	239.0	3.6	239.1	3.8	99%
B1-12	123.6	6869.2	6468.2	5981.3	0.640544	0.005138	25.237050	0.828989	0.280119	0.007536	4602.8	11.7	3317.4	32.2	1592.0	38.0	29%
B1-13	34.0	3075.4	133.7	7.5	0.063114	0.000973	0.337117	0.004577	0.039537	0.000667	722.2	33.3	295.0	3.5	250.0	4.1	83%
B1-14	71.2	4792.2	212.0	16.3	0.065040	0.001426	0.347764	0.007549	0.039061	0.000528	775.9	46.3	303.0	5.7	247.0	3.3	79%
B1-15-1	20.9	2150.8	918.5	659.4	0.382842	0.003684	10.105341	0.389113	0.185729	0.006127	3843.1	14.5	2444.5	35.6	1098.2	33.3	23%
B1-15-2	21.2	2227.6	889.9	620.5	0.372084	0.003211	8.934694	0.344283	0.169723	0.005412	3800.0	13.1	2331.4	35.2	1010.6	29.8	20%
B1-16	40.0	3262.0	132.1	0.7	0.050932	0.000379	0.269343	0.005053	0.038351	0.000686	239.0	16.7	242.2	4.0	242.6	4.3	99%
B1-17	14.2	1355.0	46.8	0.3	0.050783	0.000754	0.232737	0.005856	0.033269	0.000749	231.6	35.2	212.5	4.8	211.0	4.7	99%
B1-18	32.4	2895.3	115.8	0.3	0.050545	0.000383	0.263861	0.003518	0.037858	0.000446	220.4	13.9	237.8	2.8	239.5	2.8	99%
B1-19-1	40.1	3913.4	155.0	1.2	0.050610	0.000377	0.264336	0.003918	0.037862	0.000501	233.4	16.7	238.2	3.2	239.6	3.1	99%
B1-19-2	41.3	3668.3	146.9	1.0	0.050808	0.000384	0.266954	0.003686	0.038120	0.000493	231.6	18.5	240.3	3.0	241.2	3.1	99%
B1-20	61.4	4115.8	164.9	0.8	0.050276	0.000358	0.263977	0.004632	0.038068	0.000645	209.3	21.3	237.9	3.7	240.8	4.0	98%

Note: "CQBS21-08-B1" within spot no. was abbreviated as "B1" in each one.

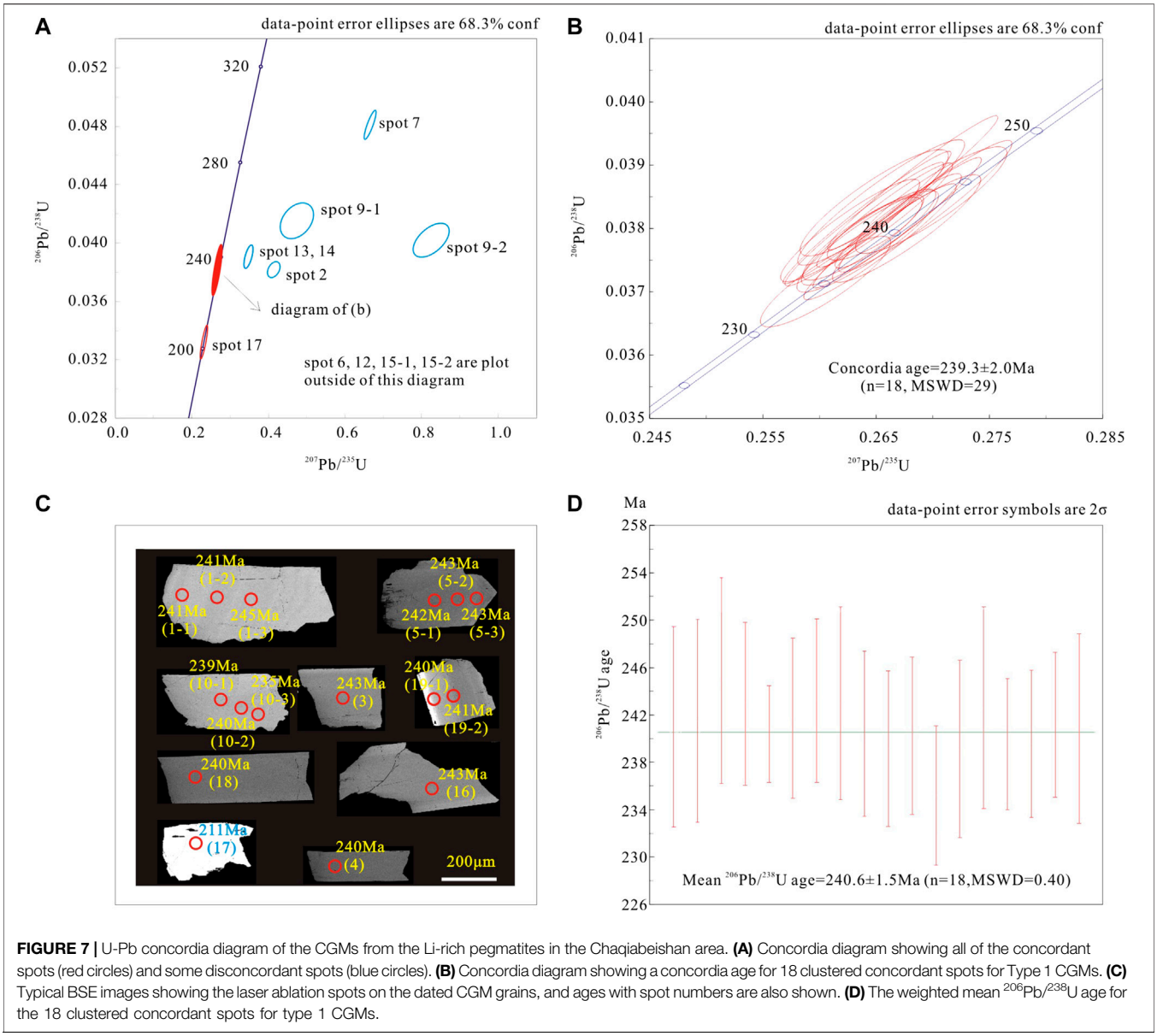

FIGURE 7 | U-Pb concordia diagram of the CGMs from the Li-rich pegmatites in the Chaqiabeishan area. **(A)** Concordia diagram showing all of the concordant spots (red circles) and some disconcordant spots (blue circles). **(B)** Concordia diagram showing a concordia age for 18 clustered concordant spots for Type 1 CGMs. **(C)** Typical BSE images showing the laser ablation spots on the dated CGM grains, and ages with spot numbers are also shown. **(D)** The weighted mean $^{206}Pb/^{238}U$ age for the 18 clustered concordant spots for type 1 CGMs.

the analyzed spots within the CGMs (**Figure 5**). Thus, we excluded the discordant dating analyses that were possibly affected by the presence of microscale inclusions, possible metamictization, or microfractures from concordia age calculation. All of the concordant dating analyses had sufficiently high U contents (1,355.0–7,597.8 ppm; **Table 2**) and very low common Pb concentrations (0.0–1.2 ppm; **Table 2**), indicating that the influence of common Pb is likely insignificant and that the U-Pb dating of such CGMs grains can provide reliable ages.

Nineteen data points with an age concordance of >98% were plotted on the U-Pb concordia diagram (**Figure 7A**). Eighteen of the data points (i.e., spots 1-1, 1-2, 1-3, 3, 4, 5-1, 5-2, 5-3, 8, 10-1, 10-2, 10-3, 11, 16, 17, 18, 19-1, 19-2, and 20) for the Type 1 CGMs have close $^{206}Pb/^{238}U$ ages ranging from 235.2 Ma to 244.9 Ma, and spot no. 17 on a Type 2 CGM has a younger $^{206}Pb/^{238}U$ age of 211.0 ± 4.7 Ma. Moreover, among these eighteen Type 1 columbite spots, the $^{206}Pb/^{238}U$ ages of the rims of the individual columbite are similar to those of the core. For example, 241.0 Ma, 241.5 Ma, and 244.9 Ma ages of spots 1-1, 1-2, and 1-3, respectively, are similar within an individual columbite grain (no. 1), indicating that there is no age variation within an individual CGM grain.

Laser Ablation-Inductively Coupled Plasma Mass Spectrometry Trace Element Analysis

All of the spots on the LA-ICP-MS dated CGM separates were simultaneously analyzed for trace element concentrations. The results are presented in **Supplementary Table S1**. Because the

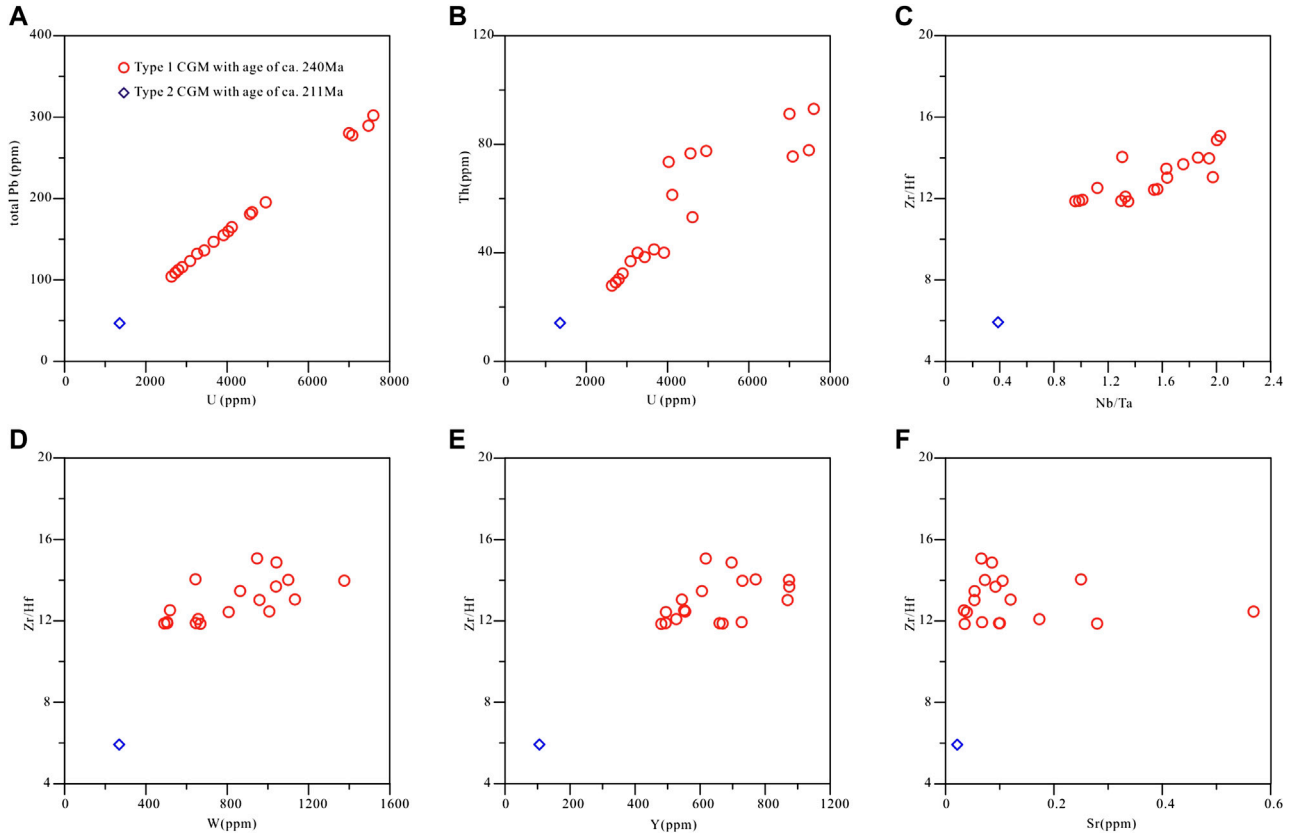

FIGURE 8 | Binary plots for the CGMs from the Li-rich pegmatites in the Chaqiabeishan area. **(A)** Pb vs. U; **(B)** Th vs. U; **(C)** Zr/Hf vs. Nb/Ta; **(D)** Zr/Hf vs. W; **(E)** Zr/Hf vs. Y; **(F)** Zr/Hf vs. Sr.

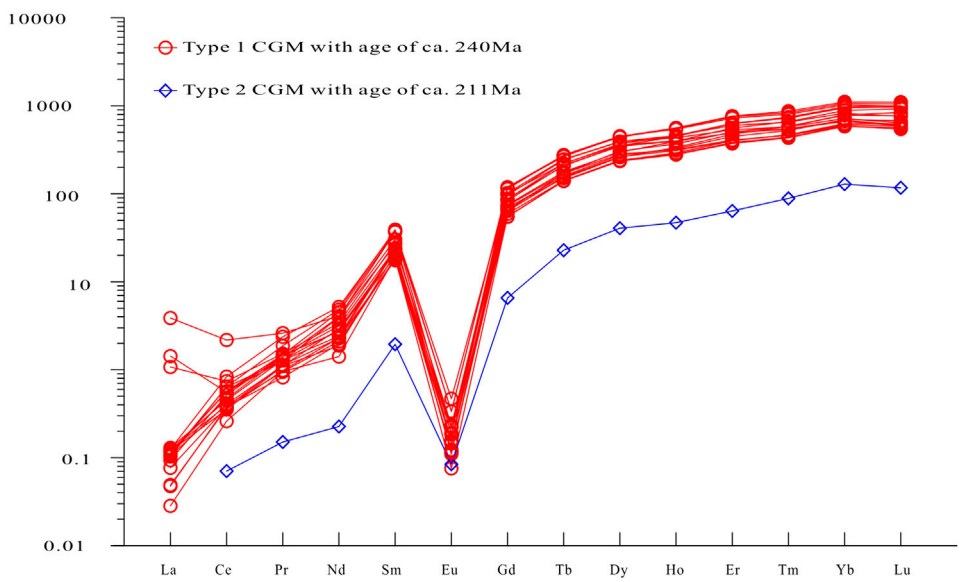

FIGURE 9 | Chondrite-normalized REE patterns for the CGMs from the Li-rich pegmatites in the Chaqiabeishan area. Chondrite normalization values are from Boynton (1984).

discordant dating analyses (i.e., spots 2, 6, 7, 9-1, 9-2, 12, 13, 14, 15-1, and 15-2) were obviously affected by the presence of microscale inclusions, microfractures, or possible metamictization, the results of the LA-ICP-MS trace element analysis are not considered to be reliable and were excluded in this study. The nineteen trace element data points with U-Pb age concordance of >98% are discussed in this study. Overall, the U and Pb concentrations of the analyzed CGMs show an excellent positive correlation (**Figure 8A**), and the U and Th concentrations also exhibit a positive correlation (**Figure 8B**). The chondrite-normalized rare earth element (REE) patterns for the CGMs invariably show depleted light rare earth elements (LREEs), strongly negative Eu anomalies, and enriched heavy rare earth element (HREE) patterns (**Figure 9**). All of the analyzed CGMs are characterized by relatively low Rb (0.0–2.0 ppm), Sr (0.0–0.6 ppm), Pb (46.8–302.1 ppm), and total REE contents and relatively high Y (105.6–874.2 ppm), Zr (1,460.8–5,483.7 ppm), U (3,913.4–3,668.3 ppm), and Th (14.2–93.1 ppm). Moreover, all of the trace element contents are basically invariable from the rim to the core within an individual CGM grain (i.e., nos. 1, 5, 10, and 19).

DISCUSSION

Genetic and Geochemical Evolutions of CGMs

The lower Mn# values and relatively low Ta# values are indicated by a dark BSE response for the analyzed CGMs grains (**Figures 5** and **6**) (Xie et al., 2019). According to the Ta# vs. Mn# quadrilateral diagram in **Figure 6**, Type 1 CGMs are columbite (Mn), the bright patches in Type 2 CGMs are tantalite (Mn), and the dark patches in Type 2 CGMs are also columbite (Mn) (e.g., spot no. 15-2). The bright patches in Type 2 CGMs are generally richer in Mn and Ta than Type 1 CGMs (**Figure 6**). The overall compositional change from Type 1 CGMs to Type 2 CGMs is consistent with the typical evolutionary trend described for many lithium-cesium-tantalum (LCT) pegmatites; e.g., Separation Rapids Tindle and Breaks, 2000), Jálama (Llorens and Moro, 2012), and Kolmozero (Badanina et al., 2015), are similar to the complex spodumene trend described by Černý and Ercit (1989) and shown in **Figure 6**. Generally, the increase in the Ta# values documents a local evolution or a magmatic/hydrothermal transition within the system (Breiter et al., 2017). Therefore, Type 2 CGMs should have formed later than Type 1 CGMs, and Type 2 GCMs may be a metasomatic product of certain Type 1 CGMs which may have suffered the late hydrothermal metasomatism of boundary layer liquids excluded from original pegmatitic melt proposed by London (2018). The irregular bright patches indicate metasomatic replacement processes (e.g., Badanina et al., 2015).

Moreover, based on the LA-ICP-MS trace element analysis (**Supplementary Table S1**), Type 1 CGMs do not show distinct trace element content variations from core to rim within an individual grain (**Figure 8**). According to the only one set of trace element data available for Type 2 CGMs (i.e., no. 17), it is roughly thought that the bright BSE image patches in Type 2 CGMs (i.e., no. 17) have lower U, Th, Pb, and W, Y, and Sr contents, lower Nb/Ta and Zr/Hf ratios (**Figure 8**), and lower total REE contents (**Figure 9**) than those of Type 1 CGMs. Moreover in both types, Nb and Zr are enriched in the least fractionated rocks, and Ta and Hf predominate in the most fractionated pegmatites (Černý and Ercit, 1985; Linnen and Cuney, 2005; Stepanov et al., 2014). Thus, it was roughly argued that Type 2 CGMs represent the later hydrothermal metasomatism products of Type 1 CGMs. The decreasing concentrations of U and Pb in the late-stage CGMs were explained as the crystallization of microlite by Badanina et al., (2015) (**Figures 8A,B**), although we did not observe any microlite in the pegmatites we studied. Perhaps, there are other reasons for the depletion of U and Pb in Type 2 CGMs. The main trend in the REE variation from the early Type 1 CGMs to the late Type 2 CGMs exhibits decreasing total REE contents and decreasing negative Eu anomalies, which is typical of late differentiates of a granitic volatile-rich magma. The variations in the chemical compositions of the different generations of CGMs can be explained by the evolution of the mineral-forming environment from a magmatic melt to a hydrothermal-metasomatic fluid (e.g., Badanina et al., 2015). According to the argument of London (2018), the boundary layer liquid is the last silicate liquid in the pegmatite-forming environment. And at their most fractionated stage, this aqueous fluid is enriched with weight-percent levels of incompatible volatile elements such as Li, Rb, Cs, and B for the LCT family and then might disperse these elements within the pegmatites (London, 2018). So, it must be reasonable that some minerals of rare elements, such as spodumene, tourmaline, and even Type 2 CGMs, are products from hydrothermal metasomatism.

Unfortunately, only one set of trace element data for Type 2 CGMs has no any statistical significance. More detailed LA-ICP-MS trace element analyses of Type 2 CGMs should be conducted in future in order to compare Type 1 and Type 2 CGMs. There is insufficient evidence for our argument regarding the chemical evolution of Type 2 CGMs.

Metallogenic Ages of Pegmatites

The data for 18 Type 1 CGM spots with an age concordance of >98% have similar $^{206}Pb/^{238}U$ ages (ranging from 235.2 Ma to 244.9 Ma). The 18 data points yield a concordant age of 239.3 ± 2.0 Ma (MSWD = 29, n = 18; **Figure 7B**) and a weighted mean $^{206}Pb/^{238}U$ age of 240.6 ± 1.5 Ma (MSWD = 0.4, n = 18; **Figure 7D**). We believe that the weighted mean $^{206}Pb/^{238}U$ age of 240.6 ± 1.5 Ma for the CGMs likely represent the magmatic emplacement age of the CGM-bearing pegmatite (**Figure 8**). Moreover, spot no. 17 on a Type 2 CGMs belongs to tantalite (Mn) rather than columbite (Mn) according its Ta# value. Type 2 CGM no. 17 experienced a different petrogenetic path than the Type 1 CGMs, but one dataset has no apparent statistical significance, and the age of 211.0 ± 4.7 Ma for grain no. 17 (Type 2 CGM) hardly represents the age of the later hydrothermal metasomatism. More detailed LA-ICP-MS dating of Type 2 CGMs should be completed in future in order to constrain the emplacement age and hydrothermal metasomatism age of the Li-rich pegmatites in the Chaqiabeishan area. But the stage of

the Middle Triassic metallogenesis of the Li-rich pegmatites (ca. 240.6 Ma) in the study area within the QM or even within the NQTB are similar to the major metallogenic stages of the Northern Tibet Li ore belt to the south and the Altay Li ore belt to the north (e.g., Hao et al., 2015; Liu et al., 2017; Wang et al., 2017; Dai et al., 2018; Xu et al., 2018; Yang et al., 2018; Tu et al., 2019), indicating that the Middle Triassic Li ore-forming potential in the study area is reasonable.

Tectonic Implications of CGM-Bearing Li-Rich Pegmatites

It is widely accepted that granitic pegmatites are the products of a highly-fractionated, volatile-rich residual magma (Jahns and Burnham, 1969; Norton, 1983; Jolliff et al., 1992; London, 1992; Webber et al., 1997; Fuertes-Fuente et al., 2000; London, 2008; London, 2018). This argument strongly relies on the granite-pegmatite relationship and the regional zonation of pegmatite groups that can reflect the distinct differentiation of granitic magmas. Although no granites are spatially linked to the Li-rich pegmatites in the Chaqiabeishan area, a granitic intrusion (I-type Narong granitic porphyry) to the south of the study area has an age approximately 245 Ma (unpublished data) similar to that of the weighted mean U-Pb age of approximately 240.6 Ma obtained for the Type 1 CGMs in this study. Thus, the CGM-bearing Li-rich pegmatites may exhibit a possible genetic link to the nearby 245 Ma granite in the Chaqiabeishan area. However, the LCT pegmatites are affiliated with S-type granites in Černý's (1991) classification, and Černý and Ercit (2005) noted that the LCT pegmatites are derived "less commonly from I-type granites." Therefore, it was hardly possible that Li-rich pegmatites were directly derived from fractional crystallization of parental magma of I-type Narong granitic porphyry. Alternatively, an anatectic origin has been proposed by several authors (Martin and De Vito, 2005; Konzett et al., 2018a; Konzett et al., 2018b; London, 2018; Feng et al., 2019) to explain the formation of LCT pegmatites without parental granitic plutons, although more detailed research studies regarding the genesis of the pegmatites should be accomplished in future.

In addition, it has been proposed that the formation of rare metal-enriched pegmatites may be related to orogenic processes (Černý, 1991) and can be used to trace the geotectonic evolution of a region (Lv et al., 2012). In many cases, LCT pegmatites are likely formed in a late/postorogenic regime (e.g., Černý, 1991; London, 2018; Zhai et al., 2019), so the Li-rich pegmatites in the Chaqiabeishan area were likely formed after the collision of the QM and the south Qilian block. And the Zongwulong oceanic basin between the QM and the South Qianli block was considered to be finally closed in the Late Triassic during an intracontinental collisional orogeny (Guo et al., 2009; Peng et al., 2016; Peng et al., 2018). However, the age of 240.6 Ma for the Type 1 CGMs, which likely represents the magmatic emplacement age of the CGM-bearing pegmatite, is the Middle Triassic rather than the Late Triassic. From the Late Permian to the Middle Triassic (240–254 Ma), a series of island arc granitoids were emplaced in the Tianjun and Wulan areas from the central to the eastern parts of the QM, including the 246 Ma Tianjunnanshan granites (Guo et al., 2009), the 254 Ma Xugeigou granite, the 251 Ma Qiluoshan granodiorite, the 249 Ma Chahannuo hornblende diorite, the 248 Ma Chahannuo granite, the 240 Ma Chahanhe granite, and the 250–244 Ma Shailekeguolei granodiorite (Wu et al., 2009; Wu et al., 2019), and 245 Ma Narong granitic porphyry (unpublished data). This stage of granitic plutonism (240–254 Ma) was considered to be related to the southward subduction of the Zongwulong oceanic plate (Wu et al., 2019). Therefore, it would be possibly accepted that the Li-rich granitic pegmatites and the 240–254 Ma granitoids are both tectonically controlled by the southward subduction of the Zongwulong oceanic plate because the magmatic emplacement of 240.6 Ma Li-rich granitic pegmatites in the study area was almost coeval with those of the 240–254 Ma granitoids in the QM. However, the tectonic event regarding the hydrothermal metasomatism of the Li-rich pegmatites needs further investigation, as Type 2 CGMs merely yielded only one dataset of U-Pb age and trace elements.

CONCLUSIONS

The results of the LA-ICP-MS CGMs U-Pb dating and trace element analysis, as well as EMPA analysis for CGMs from a Li-rich pegmatite dyke in the Chaqiabeishan area suggest the following conclusions.

The CGMs within the Li-rich pegmatites in the Chaqiabeishan area can be divided into magmatic Type 1 and hydrothermal metasomatic Type 2 CGMs. The Type 1 CGMs commonly have lower Ta# values, Mn# values, U, Th, Pb, W, Y, and Sr contents, Nb/Ta ratios, and Zr/Hf ratios than the Type 2 CGMs.

The Type 1 CGMs yielded an LA-ICP-MS U-Pb weighted a mean $^{206}Pb/^{238}U$ age of 240.6 ± 1.5 Ma based on 18 concordant ages, which represents the magmatic emplacement age of the Li-rich pegmatites; meanwhile, one spot on a Type 2 CGM yielded a $^{206}Pb/^{238}U$ age of 211.0 ± 4.7 Ma, which has no any statistical significance and hardly represents the hydrothermal metasomatism age of the Li-rich pegmatites. Data regarding Type 2 CGMs are reported in this study for future research studies.

Based on these results and the results of previous studies, it is concluded that the 240.6 Ma Li-rich granitic pegmatites in the Chaqiabeishan area, as well as the 240–254 Ma granitoids in the QM, were both emplaced during the southward subduction of the Zongwulong Ocean Plate in the Late Permian to Middle Triassic.

DATA AVAILABILITY STATEMENT

The original contributions presented in the study are included in the article/**Supplementary Material**, further inquiries can be directed to the corresponding author.

AUTHOR CONTRIBUTIONS

TP is responsible for writing original manuscript. Q-FD is responsible for copyright and revising the manuscript. XZ is responsible for drawing figures and data arrangement. S-PL

is responsible for basic data and maps. JH is responsible for sampling. LC is responsible for field work and lab work.

FUNDING

This work was supported by the Special Funding for Qinghai scholars (Grant Number QHS201802), National Natural Science Foundation of China (Grant Number 41572056) and Opening Foundation of Key Laboratory of Mineral Resources Evaluation in Northeast Asia, Ministry of Natural Resources of the People's Republic of China.

ACKNOWLEDGMENTS

We are grateful to Mr. Zhen-Hui Cao at the Wuhan Microbeam Analysis Technology Co., Ltd. for his help with the EPMA work and Prof. Chang-Zhi Wu from the State Key Laboratory for Mineral Deposits Research, Department of Earth Sciences in Nanjing University for their help with LA–ICP–MS CGMs dating and the trace element analysis. We also want to thank Jian-Ping Zheng for his assistance during field work. We thank the Editor-in-Chief and two reviewers for their thoughtful reviews. His constructive, stimulating and valuable comments and suggestions helped improve the manuscript significantly. We thank LetPub (www.letpub.com) for its linguistic assistance during the preparation of this manuscript.

SUPPLEMENTARY MATERIAL

The Supplementary Material for this article can be found online at: https://www.frontiersin.org/articles/10.3389/feart.2020.606951/full#supplementary-material.

REFERENCES

Badanina, E. V., Sitnikova, M. A., Gordienko, V. V., Melcher, F., Gäbler, H. E., Lodziak, J., et al. (2015). Mineral chemistry of columbite–tantalite from spodumene pegmatites of Kolmozero, Kola Peninsula (Russia). *Ore Geol. Rev.* 64, 720–735. doi:10.1016/j.oregeorev.2014.05.009

Boynton, W. V. (1984). "Geochemistry of the rare earth elements: meteorites studies, Henderson, P.," in *Rare earth element geochemistry*. Editor P. Henderson (New York, NY: Elservier), 63–114.

Breiter, K., Vaňková, M., Galiová, M. V., Korbelová, Z., and Kanický, V. (2017). Lithium and trace-element concentrations in triotahedral micas from granites of different geochemical types measured via laser ablation ICP-MS. *Mineral. Mag.* 81 (1), 15–33. doi:10.1180/minmag.2016.080.137

Černý, P., and Ercit, T. S. (1989). "Mineralogy of niobiumand tantalum: crystal chemical relationships, paragenetic aspects and their economic implications," in *Lanthanides, tantalum and niobium*. Editors P. Möller, P. Černý, and F. Saupé (Berlin, Germany: Springer), 27–79.

Černý, P., and Ercit, T. S. (1985). Some recent advances in the mineralogy and geochemistry of Nb and Ta in rare-element granitic pegmatites. *Bull. Mineral.* 108, 499–532. doi:10.3406/bulmi.1985.7846

Černý, P., and Ercit, T. S. (2005). The classification of granitic pegmatites revisited. *Can. Mineral.* 43, 2005–2026. doi:10.2113/gscanmin.43.6.2005

Černý, P. (1991). Rare-element granitic pegmatites. Part II: regional to global environments and petrogenesis. *Geosci. Can.* 18, 2.

Che, X. D., Wang, R. C., Wu, F. Y., Zhu, Z. Y., Zhang, W. L., Hu, H., et al. (2019). Episodic Nb–Ta mineralisation in South China: constraints from *in situ* LA–ICP–MS columbite–tantalite U–Pb dating. *Ore Geol. Rev.* 105, 71–85. doi:10.1016/j.oregeorev.2018.11.023

Che, X. D., Wu, F. Y., Wang, R. C., Gerdes, Axel., Ji, W. Q., Zhao, Z. H., et al. (2015). *In situ* U-Pb isotopic dating of columbite-tantalite by LA-ICP-MS. *Ore Geol. Rev.* 65, 979–989. doi:10.1016/j.oregeorev.2014.07.008

Chen, N. S., Gong, S. L., Sun, M., Li, X. Y., Long, X. P., Wang, Q. Y., et al. (2009). Precambrian evolution of the Quanji block, northeastern margin of Tibet: insights from zircon U-Pb and Lu-Hf isotope compositions. *J. Asian Earth Sci.* 35, 367–376. doi:10.1016/j.jseaes.2008.10.004

Chen, N. S., Zhang, L., Sun, M., Wang, Q. Y., and Kusky, T. M. (2012). U-Pb and Hf isotopic compositions of detrital zircons from the paragneisses of the Quanji Massif, NW China: implications for its early tectonic evolutionary history. *J. Asian Earth Sci.* 55, 110–130. doi:10.1016/j.jseaes.2012.04.006

Dai, H. Z., Wang, D. H., Liu, L. J., Yu, Y., Dai, J. J., and Fu, X. F. (2018). Geochronology, geochemistry and their geological significance of No. 308 pegmatite vein in the Jiajika deposit, western Sichuan, China. *Earth Sci.* 43 (10), 3664–3681. doi:10.3799/dqkx.2018.528

Ding, Q. F., Jiang, S. Y., and Sun, F. Y. (2014). Zircon U–Pb geochronology, geochemical and Sr–Nd–Hf isotopic compositions of the Triassic granite and diorite dikes from the Wulonggou mining area in the Eastern Kunlun Orogen, NW China: petrogenesis and tectonic implications. *Lithos.* 205, 266–283. doi:10.1016/j.lithos.2014.07.015

Ding, Q. F., Liu, F., and Yan, W. (2015). Zircon U–Pb geochronology and Hf isotopic constraints on the petrogenesis of early triassic granites in the wulonggou area of the eastern Kunlun orogen, northwest China. *Int. Geol. Rev.* 57, 1735–1754. doi:10.1080/00206814.2015.1029541

Feng, Y. G., Liang, T., Zhang, Z., Wang, Y. Q., Zhou, Y., Yang, X. Q., et al. (2019). Columbite U-Pb geochronology of kalu'an lithium pegmatites in northern Xinjiang, China: implications for genesis and emplacement history of rare-element pegmatites. *Minerals* 9, 456. doi:10.3390/min9080456

Fuertes-Fuente, M., Martin-Izard, A., Boiron, M. C., and Vinuela, J. M. (2000). P-T path and evolution in the franquiera granitic pegmatite, central galicia, northwestern Spain. *Can. Mineral.* 38, 1163–1175. doi:10.2113/gscanmin.38.5.1163

Gao, J. F., Zhou, M. F., Lightfoot, P. C., Wang, C. Y., Qi, L., and Sun, M. (2013). Sulfide saturation and magma emplacemet in the formation of the Permian Huangshandong Ni-Cu sulfide deposit, Xinjiang, Northwestern China. *Econ. Geol.* 108, 1833–1848. doi:10.2113/econgeo.108.8.1833

Gong, S., He, C., Wang, X., Chen, N., and Kusky, T. (2019). No plate tectonic shutdown in the early Paleoproterozoic: constraints from the ca. 2.4 Ga granitoids in the Quanji Massif, NW China. *J. Asian Earth Sci.* 172, 221–242. doi:10.1016/j.jseaes.2018.09.011

Gong, S. L., Chen, N.-S., Geng, H. Y., Sun, M., Zhang, L., and Wang, Q. Y. (2014). Zircon Hf isotopes and geochemistry of the early paleoproterozoic high-Sr low-Y quartz-diorite in the quanji massif, NW China: crustal growth and tectonic implications. *J. Earth Sci.* 25 (1), 74–86. doi:10.1007/s12583-014-0401-2

Gong, S. L., Chen, N. S., Wang, Q. Y., Kusky, T. M., Wang, L., Ba, J., et al. (2012). Early paleoproterozoic magmatism in the quanji massif, northeastern margin of the Qinghai Tibet plateau and its tectonic significance: LA-ICPMS U-Pb zircon geochronology and geochemistry. *Gondwana Res.* 21 (1), 152–166. doi:10.1016/j.gr.2011.07.011

Guo, A. L., Zhang, G. W., Qiang, J., Sun, Y. G., Li, G., and Yao, A. P. (2009). Indosinian Zongwulong orogenic belt on the northeastern margin of the Qinghai Tibet plateau. *Acta Petrol. Sin.* 25, 1–12. (in Chinese with English abstract)

Hao, X. F., Fu, X. F., Liang, B., Yuan, L. P., Pan, M., and Tang, Y. (2015). Formation ages of granite and X03 pegmatite vein in Jiajika, western Sichuan, and their geological significance. *Miner. Deposits.* 34 (6), 1199–1208. (in Chinese with English abstract)

He, C., Gong, S. L., Wang, L., Chen, N. S., Santosh, M., and Wang, Q. Y. (2018). Protracted postcollisional magmatism during plate subduction shutdown in

early Paleoproterozoic: insights from post-collisional granitoid suite in NW China. *Gondwana Res.* 55, 92–111. doi:10.1016/j.gr.2017.11.009

Jahns, R. H., and Burnham, C. W. (1969). Experimental studies of pegmatite genesis: I. A model for the derivation and crystallization of granitic pegmatites. *Econ. Geol.* 64, 843–864. doi:10.2113/gsecongeo.64.8.843

Jolliff, B. L., Papike, J. J., and Shearer, C. K. (1992). Petrogenetic relationships between pegmatite and granite based on geochemistry of muscovite in pegmatite wall zones, Black Hills, South Dakota, USA. *Geochem. Cosmochim. Acta.* 56, 1915–1939. doi:10.1016/0016-7037(92)90320-I

Kaeter, D., Barros, R., Menuge, J. F., and Chew, D. M. (2018). The magmatic–hydrothermal transition in rare-element pegmatites from southeast Ireland: LA-ICP-MS chemical mapping of muscovite and columbite–tantalite. *Geochem. Cosmochim. Acta.* 240, 98–130. doi:10.1016/j.gca.2018.08.024

Konzett, J., Schneider, T., Nedyalkova, L., Hauzenberger, C., Melcher, F., Gerdes, A., et al. (2018a). Anatectic granitic pegmatites from the eastern Alps: a case of variable rare-metal enrichment during high-grade regional metamorphism—I: mineral assemblages, geochemical characteristics, and emplacement ages. *Can. Mineral.* 56, 555–602. doi:10.3749/canmin.1800008

Konzett, J., Hauzenberger, C., Ludwig, T., and Stalder, R. (2018b). Anatectic granitic pegmatites from the eastern Alps: a case of variable rare metal enrichment during high-grade regional metamorphism. II: pegmatite staurolite as an indicator of anatectic pegmatite parent melt formation—a field and experimental study. *Can. Mineral.* 56, 603–624. doi:10.3749/canmin.1800011

Legros, H., Mercadier, J., Villeneuve, J., Romer, R. L., Deloule, E., Van Lichtervelde, M., et al. (2019). U-Pb isotopic dating of columbite-tantalite minerals: development of reference materials and *in situ* applications by ion microprobe. *Chem. Geol.* 512, 69–84. doi:10.1016/j.chemgeo.2019.03.001

Liao, F., Wang, Q., Chen, N., Santosh, M., Xu, Y., and Mustafa, H. A. (2018). Geochemistry and geochronology of the ~0.82 Ga high–Mg gabbroic dykes from the Quanji Massif, southeast Tarim Block, NW China: implications for the Rodinia supercontinent assembly. *J. Asian Earth Sci.* 157, 3–21. doi:10.1016/j.jseaes.2017.06.021

Liao, F., Zhang, L., Chen, N., Sun, M., Santosh, M., Wang, Q., et al. (2014). Geochronology and geochemistry of meta-mafic dykes in the Quanji Massif, NW China: Paleoproterozoic evolution of the Tarim Craton and implications for the assembly of the Columbia supercontinent. *Precambrian Res.* 249, 33–56. doi:10.1016/j.precamres.2014.04.015

Linnen, R. L., and Cuney, M. (2005). "Granite-related rare-element deposits and experimental constraints on Ta-Nb-W-Sn-Zr-Hf mineralization," in *Rare-element geochemistry and mineral Deposits*. Editors R. L. Linnen and I. M. Samson (St. John's, Newfoundland, Canada: Geological Association of Canada), 45–68.

Linnen, R. L., Samson, I. M., Williams-Jones, A. E., and Chakhmouradian, A. R. (2014). "Geochemistry of the rare-earth element, Nb, Ta, Hf, and Zr deposits," in *Treatise on geochemistry*. 2nd Edn. Editors K. Holland and Turekian (Oxford, UK: Elsevier), 543–564.

Linnen, R. L., Van Lichtervelde, M., and Černý, P. (2012). Granitic pegmatites as sources of strategic metals. *Elements.* 8, 275–280. doi:10.2113/gselements.8.4.275

Liu, L. J., Wang, D. H., Hou, K. J., Tian, S. H., Zhao, Y., Fu, X. F., et al. (2017). Application of lithium isotope to Jiajika new No.3 pegmatite litium polymetallic vein in Sichuan. *Earth Sci. Front.* 24 (5), 167–171. doi:10.13745/j.esf.yx.2017-1-16

Liu, Y. S., Hu, Z. C., Gao, S., Gunther, D., Xu, J., Gao, C. G., et al. (2008). *In situ* analysis of major and trace elements of anhydrous minerals by LA-ICP-MS without applying an internal standard. *Chem. Geol.* 257 (1–2), 34–43. doi:10.1016/j.chemgeo.2008.08.004

Llorens, T., and Moro, M. C. (2012). Oxide minerals in the granitic cupola of the Jálama Batholith, Salamanca, Spain. Part I: accessory Sn, Nb, Ta and Ti minerals in leucogranites, aplites and pegmatites. *J. Geosci.* 57, 25–43. doi:10.3190/jgeosci.113

London, D. (2018). Ore-forming processes within granitic pegmatites. *Ore Geol. Rev.* 101, 349–383. doi:10.1016/j.oregeorev.2018.04.020

London, D. (2008). *The Canadian mineralogist*. London, UK: Special Publication, 347.

London, D. (1992). The application of experimental petrology to the genesis and crystallization of granitic pegmatites. *Can. Mineral.* 30, 499–540.

Lu, S. N., Li, H. K., Zhang, C. L., and Niu, G. H. (2008). Geological and geochronological evidence for the precambrian evolution of the Tarim Craton and surrounding continental fragments. *Precambrian Res.* 160 (1/2), 94–107. doi:10.1016/j.precamres.2007.04.025

Lu, S. N., Yu, H. F., Li, H. K., Guo, K. Y., Wang, H. C., Jin, W., et al. (2006). Research on Precambrian major problems in Chinese. (Beijing: Geological Publishing House), 1–197. (in Chinese).

Ludwig, K. R. (2003). User's manual for isoplot/ex, version 3.00: a geochronological toolkit for microsoft Excel. *Berkeley Geochronol. Cent. Spec. Publ.* 4, 1–70.

Lv, Z. H., Zhang, H., Tang, Y., and Guan, S. J. (2012). Petrogenesis and magmatic–hydrothermal evolution time limitation of Kelumute No. 112 pegmatite in Altay, Northwestern China: evidence from zircon U Pb and Hf isotopes. *Lithos.* 154, 374–391. doi:10.1016/j.lithos.2012.08.005

Martin, R. F., and De Vito, C. (2005). The patterns of enrichment in felsic pegmatites ultimately depend on tectonic setting. *Can. Mineral.* 43, 2027–2048. doi:10.2113/gscanmin.43.6.2027

Mustafa, H. A., Wang, Q., Chen, N., Liao, F., Sun, M., and Salih, M. A. (2016). Geochemistry of metamafic dykes from the Quanji massif: petrogenesis and further evidence for oceanic subduction, late paleoproterozoic, NW China. *J. Earth Sci.* 27, 529–544. doi:10.1007/s12583-015-0659-z

Norton, J. J. (1983). Sequence of mineral assemblages in differentiated granitic pegmatites. *Econ. Geol.* 78, 854–874. doi:10.2113/gsecongeo.78.5.854

Pan, T., Li, S. P., Ren, H., and Wang, B. Z. (2020). Metallogenic conditions and prospecting potential of lithium polymetalloic deposits in north Qaidam basin. *Miner. Explor.* 11 (6), 1101–1116. (in Chinese with English abstract)

Pang, J. Z., Yu, J. X., Zheng, D. W., Wang, W. T., Ma, Y., Wang, Y. Z., et al. (2019). Neogene expansion of the qilian Shan, north Tibet: implications for the dynamic evolution of the Tibetan plateau. *Tectonics.* 38, 1018–1032. doi:10.1029/2018TC005258

Peng, Y., Ma, Y. S., Liu, C. L., Sun, J. P., and Shao, P. C. (2016). Geological characteristics and tectonic significance of the Indosinian granodiorites from the Zongwulong tectonic belt in North Qaidam. *Earth Sci. Front.* 23, 206–221. doi:10.13745/j.esf.2016.02.020

Peng, Y., Zhang, Y. S., Sun, J. P., Xing, E. Y., and Yu, H. T. (2018). Geochemistry of Late Carboniferous sedimentary rocks from the Zongwulong structural belt and adjacent areas, Qaidam Basin, China: implications for provenance and tectonic setting. *Geosci. J.* 22 (2), 287–301. doi:10.1007/s12303-017-0032-6

QGSI (2020). *Internal reports of ore exploration of Li-rich pegmatites in chaiqiabeishan area in Tianjun county, Qinghai Province*.

Romer, R. L. (2003). Alpha-recoil in U-Pb geochronology: effective sample size matters. *Contrib. Mineral. Petrol.* 145, 481–491. doi:10.1007/s00410-003-0463-0

Romer, R. L., Smeds, S. A., and Černý, P. (1996). Crystal-chemical and genetic controls of U-Pb systematics of columbite-tantalite. *Mineral. Petrol.* 57, 243–260. doi:10.1007/BF01162361

Romer, R. L., and Wright, J. E. (1992). U-Pb dating of columbites: a geochronologic tool to date magmatism and ore deposits. *Geochem. Cosmochim. Acta.* 56, 2137–2142. doi:10.1016/0016-7037(92)90337-I

Smith, S. R., Foster, G. L., Romer, R. L., Tindle, A. G., Kelley, S. P., Noble, S. R., et al. (2004). U-Pb columbite-tantalite chronology of rare-element pegmatites using TIMS and laser ablation multi collector-ICP-MS. *Contrib. Mineral. Petrol.* 147, 549–564. doi:10.1007/s00410-003-0538-y

Song, S. G., Niu, Y. L., Su, L., Zhang, C., and Zhang, L. F. (2014). Continental orogenesis from ocean subduction, continent collision/subduction, to orogen collapse, and orogen recycling: the example of the north Qaidam UHPM belt, NW China. *Earth Sci. Rev.* 129, 59–84. doi:10.1016/j.earscirev.2013.11.010

Song, S. G., Niu, Y. L., Zhang, G. B., and Zhang, L. F. (2018). *Two epochs of eclogite metamorphism link 'cold' oceanic subduction and 'hot' continental subduction, the north Qaidam UHP belt, NW China*. London, UK: Geological Society Special Publications, 474.

Stepanov, A., Mavrogenes, J. A., Meffre, S., and Davidson, P. (2014). The key role of mica during igneous concentration of tantalum. *Contrib. Mineral. Petrol.* 167, 499–1009. doi:10.1007/s00410-014-1009-3

Timofeev, A., Migdisov, A. A., and Williams-Jones, A. E. (2017). An experimental study of the solubility and speciation of tantalum in fluoride-bearing aqueous

solutions at elevated temperature. *Geochem. Cosmochim. Acta.* 197, 294–304. doi:10.1016/j.gca.2016.10.027

Tindle, A. G., and Breaks, F. W. (2000). Columbite–tantalite mineral chemistry from rare-element granitic pegmatites: Separation Lake area, N.W. Ontario, Canada. *Mineral. Petrol.* 70, 165–198. doi:10.1007/s007100070002

Tu, Q. J., Li, J. K., Wang, G., and Ma, H. C. (2019). Mineralization comparisons of the major pegmatite type spodumene deposits and their prospecting potential in West China. *Geological Surv. China.* 6 (6), 35–47. (in Chinese with English abstract)

Van Lichtervelde, M., Salvi, S., Beziat, D., and Linnen, R. L. (2007). Textural features and chemical evolution in tantalum oxides: magmatic versus hydrothermal origins for Ta mineralization in the Tanco Lower pegmatite, Manitoba, Canada. *Econ. Geol.* 102, 257–276. doi:10.2113/gsecongeo.102.2.257

Wang, B. Z., Han, J., Xie, X. L., Chen, J., Wang, T., Xue, W. W., et al. (2020). Discovery of the indosinian (Beryl-bearing) spodumene pegmatitic dike swarm in the chakaibeishan area in the northeastern margin of the Tibetan plateau: implications for Li-Be mineralization. *Geotect. Metallogenia.* 44 (1), 69–79. (in Chinese with English abstract)

Wang, D. H., Liu, L. J., Dai, H. Z., Liu, S. B., Hou, J. L., and Wu, X. S. (2017). Discussion on particularity and prospecting direction of large and super-large spodumene deposits. *Earth Sci.* 42 (12), 2243–2257. doi:10.3799/dqkx.2017.142

Wang, L., Johnston, S. T., and Chen, N. S. (2019). New insights into the Precambrian tectonic evolution and continental affinity of the Qilian block: evidence from geochronology and geochemistry of metasupracrustal rocks in the North Wulan terrane. *Geol. Soc. Am. Bull.* 131, 1723–1743. doi:10.1130/B35059.1

Wang, L., Wang, H., He, C., Chen, N. S., Santosh, M., Sun, M., et al. (2016). Mesoproterozoic continental breakup in NW China: evidence from gray gneisses from the North Wulan terrane. *Precambrian. Res.* 281, 521–536. doi:10.1016/j.precamres.2016.06.016

Wang, Q. Y., Dong, Y. J., Pan, Y. M., Liao, F. X., and Guo, X. W. (2018). Early paleozoic granulite-facies metamorphism and magmatism in the northern wulan terrane of the quanji massif: implications for the evolution of the Proto-Tethys ocean in northwestern China. *J. Earth Sci.* 29, 1081–1101. doi:10.1007/s12583-018-0881-6

Webber, K. L., Falster, A. U., Simmons, W. B., and Foord, E. E. (1997). The role of diffusion controlled oscillatory nucleation in the formation of line rock in pegmatite-aplite dikes. *J. Petrol.* 38, 1777–1791.

Wu, C. L., Wooden, J. L., Robinson, P. T., Gao, Y. H., Wu, S. P., Chen, Q. L., et al. (2009). Geochemistry and zircon SHRIMP U-Pb dating of granitoids from the west segment of the North Qaidam. *Sci. China Earth Sci.* 52, 1771–1790. doi:10.1007/s11430-009-0147-3

Wu, C. L., Wu, D., Mattinson, C., Lei, M., and Chen, H. J. (2019). Petrogenesis of granitoids in the Wulan area: magmatic activity and tectonic evolution in the North Qaidam, NW China. *Gondwana Res.* 67, 147–171. doi:10.1016/j.gr.2018.09.010

Xiao, W. J., Windley, B. F., Yong, Y., Yan, Z., Yuan, C., Liu, C. Z., et al. (2009). Early paleozoic to devonian multiple-accretionary model for the qilian Shan, NW China. *J. Asian Earth Sci.* 35, 323–333. doi:10.1016/j.jseaes.2008.10.001

Xie, L., Liu, Y., Wang, R. C., Hu, H., Che, X. D., and Xiang, L. (2019). Li–Nb–Ta mineralization in the Jurassic Yifeng granite-aplite intrusion within the Neoproterozoic Jiuling batholith, south China: a fluid-rich and quenching ore-forming process. *J. Asian Earth Sci.* 185, 104047. doi:10.1016/j.jseaes.2019.104047

Xiong, F., Ma, C., Zhang, J., Liu, B., and Jiang, H. (2014). A reworking of old continental lithosphere: an important crustal evolutionmechanism in orogenic belts, as evidenced by Triassic I-type granitoids in the East Kunlun orogen, Northern Tibetan Plateau. *J. Geol. Soc.* 171, 847–863. doi:10.1144/jgs2013-038

Xu, Z. Q., Wang, R. C., Zhao, Z. B., and Fu, X. F. (2018). On the structural backgrounds of the large-scale "hard-rock type" lithium ore belts in China. *Acta Geol. Sin.* 92 (6), 1091–1106. (in Chinese with English abstract)

Xu, Z. Q., Yang, J. S., Wu, C. L., Li, H. B., Zhang, J. X., Qi, X. X., et al. (2006). Timing and mechanism of formation and exhumation of the Northern Qaidam ultrahigh-pressure metamorphic belt. *J. Asian Earth Sci.* 28, 160–173. doi:10.1016/j.jseaes.2005.09.016

Yan, Q., Qiu, Z., Wang, H., Wang, M., Wei, X., Li, P., et al. (2018). Age of the Dahongliutan rare metal pegmatite deposit, West Kunlun, Xinjiang (NW China): constraints from LA-ICP-MS U-Pb dating of columbite-(Fe) and cassiterite. *Ore Geol. Rev.* 100, 561–573. doi:10.1016/j.oregeorev.2016.11.010

Yang, F. Q., Zhang, Z. L., Wang, R., Li, Q., Ding, J. G., Su, Z. H., et al. (2018). Geological characteristics and metallogenesis of rare metal deposits in Altay, Xinjiang. *Geotect. Metallogenia.* 42 (6), 1010–1026. (in Chinese with English abstract)

Zhai, M. G., Wu, F. Y., Hu, R. Z., Jiang, S. Y., Li, W. C., Wang, R. C., et al. (2019). Critical metal mineral resources: current reseach status and scientific issues. *Bull. Natl. Nat. Sci. Found. China.* 2, 106–111. (in Chinese with English abstract)

Zhang, H. J., Wang, X. L., Wang, X., and Zhou, H. R. (2016). U-Pb zircon ages of tuff from the Hongzaoshan Formation, Quanji Group, in the north margin of Qaidam Basin, NW China, and their geological significances. *Earth Sci. Front.* 23, 202–218. doi:10.13745/j.esf.2016.06.014

Zhang, J. X., Mattinson, C. G., Yu, S. Y., and Li, Y. S. (2014a). Combined rutile-zircon thermometry and U-Pb geochronology: new constraints on early paleozoic HP/UHT granulite in the south altyn tagh, north Tibet, China. *Lithos.* 200/201, 241–257. doi:10.1016/j.lithos.2014.05.006

Zhang, J. X., Yu, S. Y., and Mattinson, C. G. (2017). Early paleozoic polyphase metamorphism in northern Tibet, China. *Gondwana Res.* 41, 267–289. doi:10.1016/j.gr.2015.11.009

Zhang, L., Ba, J., Chen, N. S., Wang, Q. Y., Liao, F. X., and Li, X. Y. (2012). U-Pb age spectra and trace elements of detrital zircon from quanji group: implications for thermal events and early evolution in the basement. *J. Earth Sci.* 37, 28–42. doi:10.3799/dqkx.2012.S1.004

Zhang, L., Wang, Q. Y., Chen, N. S., Sun, M., Santosh, M., and Ba, J. (2014b). Geochemistry and detrital zircon U-Pb and Hf isotopes of the paragneiss suite from the quanji massif, SE Tarim Craton: implications for paleoproterozoic tectonics in NW China. *J. Asian Earth Sci.* 95, 33–50. doi:10.1016/j.jseaes.2014.05.014

Zhang, R. X., and Yang, S. Y. (2016). A mathematical model for determining carbon coating thickness and its application in electron probe microanalysis. *Microsc. Microanal.* 22, 1374–1380. doi:10.1017/S143192761601182X

Zhao, F. Q., Lu, S. N., and Li, H. K. (2000). "The geochemical characteristics of the Mes-Neoproterozoic granite belt in the dakendaban complex rocks of the Qaidam block," in Abstracts of the second cross strait: Qilian Mountains and its adjacent areas. Beijing, 95–97 (in Chinese).

Conflict of Interest: The authors declare that the research was conducted in the absence of any commercial or financial relationships that could be construed as a potential conflict of interest.